AIAA JOURNAL
Vol. 46, No. 9, September 2008

Flow-Induced Sound of Wall-Mounted Cylinders with Different Geometries

Stefan Becker*
University of Erlangen—Nürnberg, 91058 Erlangen, Germany
and
Christian Hahn,† Manfred Kaltenbacher,‡ and Reinhard Lerch§
University of Erlangen—Nürnberg, 91052 Erlangen, Germany

DOI: 10.2514/1.34865

The objective of this work was to investigate the influence of changes in geometry of a wall-mounted square cylinder in crossflow on the generated aerodynamic noise. The flowfield and acoustic field of several geometries are obtained and their interaction is analyzed. The results of the subset of geometries investigated indicate that the reduction in turbulent kinetic energy does not necessarily also lead to a reduction in radiated noise. Reducing the fluctuations of the stagnation point in front of the cylinder, maintaining a fixed separation line, and reducing the symmetry of the vortex street and its stability seem to be effective measures for reducing aerodynamic noise, among other known approaches.

Nomenclature

c_D	=	coefficient of drag
D	=	cylinder side length, m
f_{shed}	=	vortex shedding frequency, Hz
L	=	cylinder length, m
Re_D	=	Reynolds number based on cylinder side length D
St	=	Strouhal number
U, V, W	=	velocity components in Cartesian coordinates, m/s
U_0	=	inflow velocity, m/s
x, y, z	=	Cartesian body axes, m
δ_{99}	=	boundary-layer thickness at 99% of inflow velocity, m

I. Introduction

AERODYNAMIC sound is a major source of noise in high-speed transportation. With the increase in traffic, noise pollution is becoming an increasingly relevant topic. The sound created by the flow around cylindrical objects constitutes a major part of the total flow-induced sound. Cylindrical geometries are present in many engineering applications such as the pantographs of trains, high-rise buildings, car antennas, beams, fences, and supports in internal and external flows. Therefore, the flow around cylindrical objects has been the subject of a large number of research activities.

The majority of these investigations have been carried out for the flow around circular cylinders, dealing with the flowfield in combination with the associated sound field [1–6]. In addition, a reasonable amount of data is available for the flow around square cylinders, including the effects of varying orientation toward the flow [7–11]. Unfortunately, nearly all of them focus on two-dimensional flowfields. Concerning the three-dimensional flow around wall-mounted cylinders of finite length, little data can be found concerning the fluid mechanical aspects of this setup [12–14]. The objective of the last two preceding investigations was to obtain information about the flowfield around building structures. Therefore, the simulation of a boundary layer similar to the atmospheric layer was a crucial issue.

To the authors' knowledge, there is a total absence of data concerning the flow-induced sound of a wall-mounted square cylinder in crossflow, which is the topic of the investigations presented here. The object of our investigations was therefore twofold. First, we aimed to gain a better understanding of the physical mechanisms responsible for flow-induced noise generation and radiation in this particular setup and also to achieve reductions in the aeolian tone connected with the flow around the cylinder. Second, we aimed to provide data for both the flowfield and sound field of a wall-mounted cylinder. The data obtained are being used to fill the aforementioned gap and to validate numerical simulations of this setup [15,16].

The setup investigated in this work is displayed in Fig. 1. A rigid square cylinder with side dimension D and length L is mounted vertically on a flat wall. The cylinder has a constant aspect ratio L/D of 6. The flow over a finite length cylinder is strongly three-dimensional, due to the interaction of the tip vortex with the Kármán vortex shedding and the horseshoe vortex. The resulting flowfield strongly depends on the aspect ratio and the ratio between cylinder length L and the boundary-layer thickness [12–14]. When the aspect ratio exceeds 5 (smooth geometries), periodic spanwise vortex shedding occurs over almost the whole span, except very close to the wall. Additional separation occurs from the top of the cylinder, but the flow region behind the cylinder is dominated by the spanwise vortex shedding. The general flow structure for this case is depicted in Fig. 2.

The nature and the thickness of the boundary layer in relation to the cylinder length influence the flowfield. On approaching the cylinder, the boundary layer separates due to the adverse pressure gradient inducing vortices that are being stretched around the cylinder, forming a horseshoe vortex. The Strouhal number St related to the spanwise vortex shedding frequency increases with an increase in the ratio between cylinder length and boundary-layer thickness.

Figure 3 displays Strouhal numbers for an aspect ratio of 6 in relation to boundary-layer thickness. The thickness δ_{99} of the (in the case referred to, turbulent) boundary layer is taken to be the distance from the wall at which 99% of the freestream velocity is measured. These results are obtained in a situation in which the length of the cylinder is of the same order of magnitude as the boundary-layer thickness.

In general, the Strouhal numbers St for a square cylinder in two-dimensional flow with Reynolds numbers Re_D in the range

Presented as Paper 3430 at the 13th AIAA/CEAS Aeroacoustics Conference, Rome, Italy, 21–23 May 2007; received 28 September 2007; revision received 12 June 2008; accepted for publication 13 June 2008.

*Institute of Fluid Mechanics. Member AIAA.
†Ph.D. Student, Department of Sensor Technology, Experimental Aeroacoustics Research.
‡Department of Sensor Technology. Member AIAA.
§Head, Department of Sensor Technology.

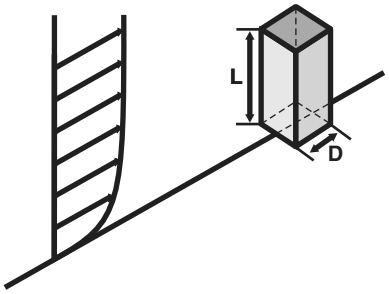

Fig. 1 Basic setup: wall-mounted square cylinder in crossflow.

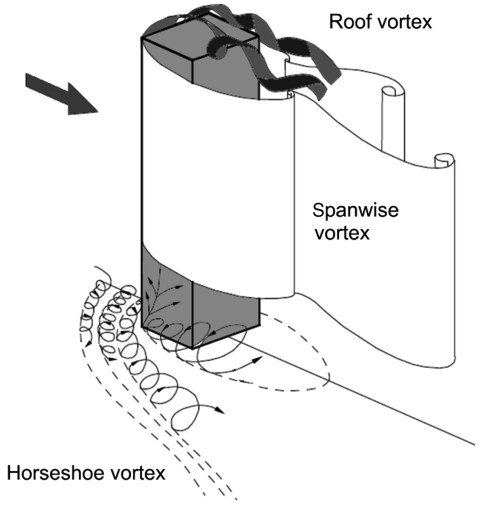

Fig. 2 Flow structure behind a square prism with aspect ratio $L/D > 5$ [12].

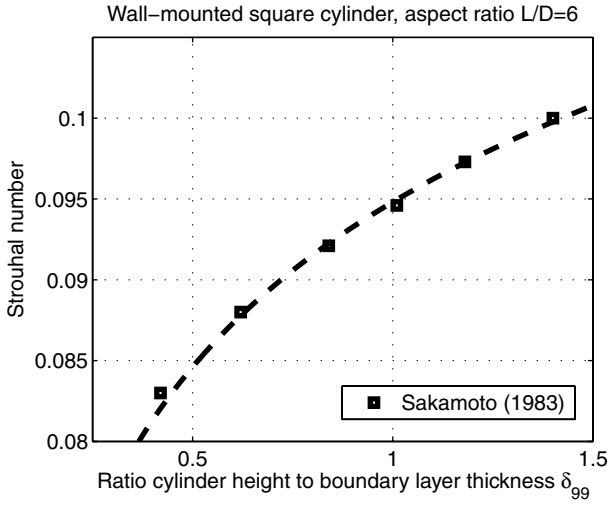

Fig. 3 Relationship between Strouhal number and ratio of cylinder length to boundary-layer thickness [13].

1.0×10^4–21.4×10^4 lie between 0.122 and 0.142 (see, for example, [10]). Published data [8] indicate a Strouhal number St of 0.132 for a Reynolds number Re_D of 10.0×10^4. However, it has to be borne in mind that in the references cited, cylinders with higher aspect ratios were used (15 and 120, compared with a ratio of 6 in our case). Additionally, measures were taken to create a two-dimensional flow pattern: for example, by using end plates, which do not correspond to the setup presented here.The intensity of the aeolian tone created by the cylinder depends on the magnitude of the pressure fluctuations on the cylinder surface and its correlation length [1,2].

An increase in noise is observed when the boundary layer separates at the leading edge and reattaches on the cylinder. This can be caused by changes in the orientation of the cylinder toward the flow [11] or when leading edges are rounded and, due to inclination of the cylinder, reattachment occurs [17]. The influence of inclination concerning tapered cylinders has been discussed by Hayashi et al. [18].

Various concepts exist to reduce the strength of the vortices shed and their correlation. Splitter plates in the wake of cylinders effectively reduce vortex shedding, depending on plate length [3,19]. Helical streaks around circular cylinders or spoilers along the cylinder's axis lead to spanwise dephased separation, thereby reducing the correlation length [3].

Overviews of the effects of the trailing-edge shape on vortex-induced vibration of plates have been given by Blake [20] and Naudascher and Rockwell [3]. Such geometries, which have been proven useful for the flow around rigid plates, might also be suitable for the design of an afterbody for a square cylinder. Using asymmetric trailing-edge shapes leads to dephased separation in the streamwise direction [3].

Additionally, the formation of the vortex street can be influenced by mass injection into the wake using external sources or by drilled holes from the front side to the rear side of the cylinder [3,21].

The major part of the paper is organized as follows: In Sec. II, the general measurement setup and the investigated geometries are presented. Section III concentrates on the influence of geometry variations on the induced sound, and in Sec. IV, the flowfield is related to the induced sound. Special consideration is given to the influence of the roof vortex on both fluid and the acoustic field in Sec. V.

II. Measurement Setup

A. Model Geometries

Different shapes are used as fore- or afterbodies on the square cylinder, and their influence on the flowfield and on the flow-induced noise is studied. Starting from the basic square-cylinder geometries with an additional elliptical forebody (outer dimensions of 20×30 mm), an elliptical afterbody with the same dimensions and a three-edged wedge (dimensions of 20×10 mm) are tested (Fig. 4). The square cylinder itself has a side length of $D = 20$ mm and a length of $L = 120$ mm.

B. Measurement Facilities

Almost all of the investigations conducted were carried out in the aeroacoustic wind tunnel of the University of Erlangen–Nürnberg in Germany (Department of Sensor Technology and Institute of Fluid Mechanics). Only measurements of the mean flowfield via laser Doppler anemometry (LDA) were performed in the aerodynamic wind tunnel at the Institute of Fluid Mechanics.

1. Measurement Setup in the Aeroacoustic Wind Tunnel

The general measurement setup for the investigations conducted in the aeroacoustic wind tunnel is shown in Fig. 5. The square cylinder is mounted on a flat plate with its front face incident to the flow.

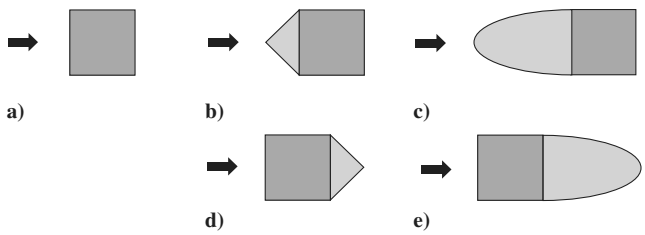

Fig. 4 Investigated geometry variations with a length $L = 120$ mm and square cylinders with a) $D = 20$ mm, b) three-edged wedge in front (dimensions 20×10 mm), c) elliptical forebody (outer dimensions 20×30 mm), d) three-edged wedge on the back side (dimensions 20×10 mm), and e) elliptical afterbody (outer dimensions 20×30 mm).

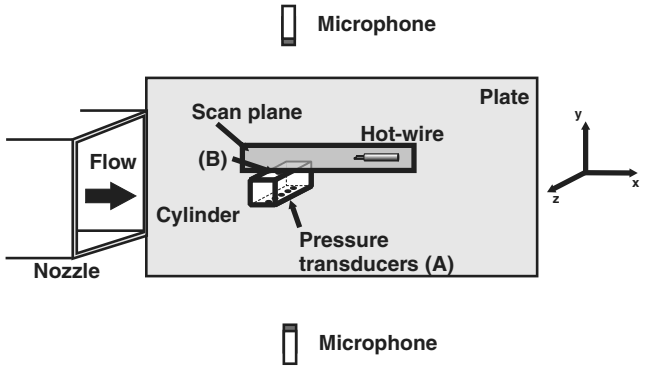

Fig. 5 Measurement setup in the aeroacoustic wind tunnel.

The orientation and aspect ratio of the cylinder remain unchanged throughout the measurements. The center of the cylinder is located 370 mm downstream of the nozzle exit cross section. The plate has a length of 1 m in the streamwise direction and a width of 660 mm in the lateral direction. The plate is flush-mounted to a nozzle that has an exit cross section of 0.25 m in the y direction times 0.33 m in the z direction, yielding a blockage ratio of about 3%. For this amount of blockage, the error can be neglected in an open wind-tunnel section [14].

The velocity field of the square cylinder is measured via hot-wire anemometry in a plane parallel to the plate at a height of $z = 60$ mm. Microphones are located on either side of the cylinder at a distance of 0.71 m away from the cylinder's center in the same plane used for velocity measurements.

The aeroacoustic wind tunnel is of the closed-return type with an open test section. The test section is integrated into an anechoic chamber, thus allowing free-field acoustic measurements without reflections from the surrounding walls. The chamber itself has an absorption coefficient of 0.9 for a frequency of 300 Hz. The wind tunnel is provided with silencers to make for a low noise level in the test section and to damp out fan noise. This wind tunnel has a maximum jet velocity of 50 m/s. With a nozzle exit diameter of 0.25×0.33 m (contraction ratio 4:1), as used in the measurements presented here, a maximum exit velocity of about 33 m/s can be obtained. Because of several turbulence grids and a honeycomb, a low turbulence level of about 0.15% is achieved.

2. Measurement Setup in the Aerodynamic Wind Tunnel

Additional measurements of the flowfield were carried out in the aerodynamic wind tunnel of the Institute of Fluid Mechanics using a two-component laser Doppler anemometer.

Here, the square cylinder is not placed on the floor of the tunnel. Instead, it is mounted in the center of a plate (thickness of 12 mm) that is located about 0.5 m above the tunnel floor and extends 1 m in the streamwise direction and 0.6 m in the lateral direction (see Fig. 6) to obtain inflow conditions similar to those in the aeroacoustic wind tunnel. At the leading edge of the plate, a NACA 0001 profile is attached. Thereby, a boundary layer with a small thickness compared with the cylinder length can be obtained. The leading edge of the plate is located 0.5 m downstream of the exit cross section of the wind tunnel.

The aerodynamic wind tunnel is also of the closed-return type. The nozzle exit cross section has a width of 1.87 m in the horizontal direction and a height of 1.4 m in the vertical direction (contraction ratio 5:1). The turbulence level of this tunnel is 0.12%.

C. Measurement Equipment

Velocity measurements in the aeroacoustic wind tunnel are carried out with a single-wire anemometer (Dantec type 55M01). The constant-temperature anemometer can be remotely traversed across the test section and is calibrated with the help of a Prandtl tube before the measurements. The accuracy of the hot-wire measurement system depends on different factors: namely, the direction of the oncoming flow, the quality of the calibration procedure, the constancy of the ambient temperature, and the measuring time and

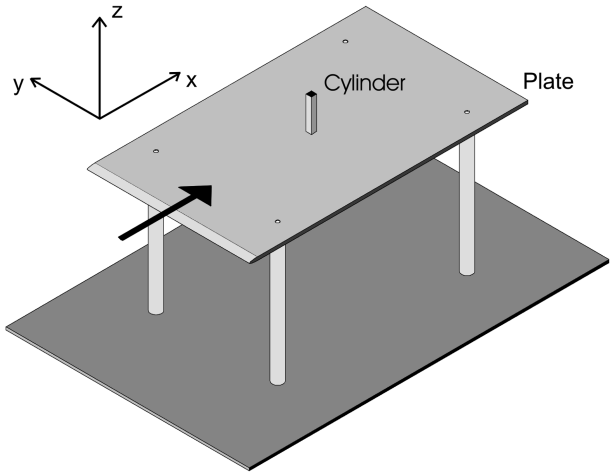

Fig. 6 Measurement setup in the aerodynamic wind tunnel.

the turbulence intensity [4]. The hot-wire anemometer measurements are performed only in the outer region of the recirculation zone behind the obstacles. Based on the statistical procedure of Bendat and Piersol [22] for a 95% confidence interval, the uncertainty of the mean velocity is less than 3% and between 5 and 10% for rms quantities in the regions of turbulence intensities from 20 to 30%.

The flow-induced noise is recorded with a $\frac{1}{2}$-in. free-field condenser microphone (B&K 4189). The directivity of the radiated sound is obtained via a sound-intensity probe (Microflown pressure-particle-velocity probe), which is calibrated in a short standing-wave tube. Local wall pressure is measured with miniature pressure transducers (Kulite LQ-125-5 SG) embedded in the cylinder's surface. All signals are recorded simultaneously with a PC using a LabView environment and a National Instruments 4472 data acquisition card.

To complement the experiments, measurements with LDA are performed. To avoid contamination of the silencers of the aeroacoustic wind tunnel due to the particle seeding necessary in the LDA technique, these measurements are carried out in a classical aerodynamic wind tunnel. The aim is to obtain detailed velocity data around the different obstacle geometries with respect to the previous aeroacoustic data. The major advantage in using LDA is to provide reliable measurements in the recirculation zone of the wake flow close to the obstacle. In the present study, a special design of a two-component LDA probe is used. This probe is specially designed for application in low-speed wind tunnels. At an outer diameter of 60 mm, it creates a measuring volume of about 75 μm in diameter at a working distance of about 400 mm. The detection of scattered light is in the direct backscatter mode. To reduce the probe's frontal area exposed to the flow, the beam path is deflected with a 45-deg mirror. An illustration of the general setup during the measurements is shown in Fig. 7.

Because all three velocity components and the turbulent fluctuations are of interest, each measurement location has to be sampled twice, first for the U and V velocity components, then with the probe rotated by 90 deg to obtain the third W component. Preliminary statistical analysis indicates that in regions with high turbulence intensities, approximately 15,000 measurements are necessary at each location for statistically significant results. This translates to a maximum measurement time of approximately 120 s at each grid point. Following the procedure outlined [22] for a 95% confidence interval, the statistical uncertainty of the mean velocity in the outer flow (far from the cylinder model) is less than 0.01% of the local mean velocity.

Within the wake of the wall-mounted cylinder, in which mean velocities can approach zero and turbulence intensities are very high, an estimate of the mean velocity measurement uncertainty is rather arbitrary. An order-of-magnitude estimate for the calculated 95% confidence interval is 1% for the mean and 1.5% for rms quantities. The LDA system measures turbulence intensities as small as 0.8% in the outer-flow region. This value represents a lower threshold for the measured turbulence intensity and includes all inaccuracies due to

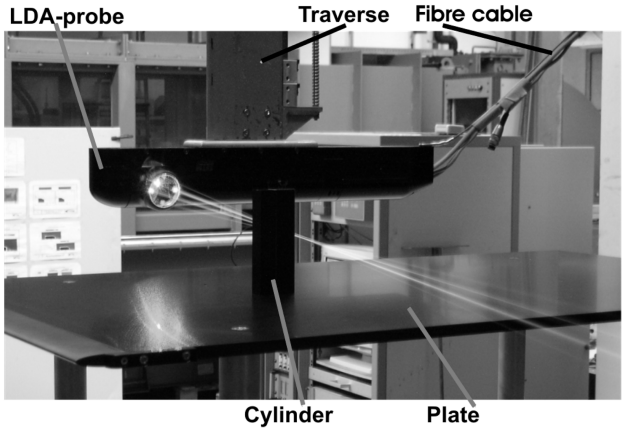

Fig. 7 LDA probe during the measurements.

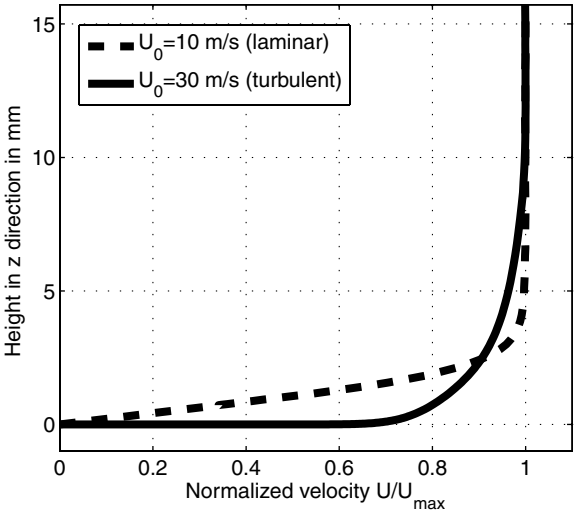

Fig. 8 Boundary-layer profiles of the aeroacoustic wind tunnel, 10*D* upstream of the cylinder's center.

the measurement technique, wind-tunnel fluctuations, and traverse system vibrations.

D. Inflow Conditions

In the aerodynamic wind tunnel, the inflow boundary profile is measured at a distance of 10*D* upstream of the cylinder's center. Measurements are carried out at $U_0 = 10$ and 30 m/s, resulting in Reynolds numbers Re_D of 12.5×10^4 and 37.6×10^4 based on the cylinder side length D. When carrying out measurements at a flow speed of 30 m/s, in both tunnels, a tripping tape is placed near the upstream end of the plate to create a well-defined turbulent boundary layer. The inflow boundary layers of the aeroacoustic wind tunnel are displayed in Fig. 8. A displacement thickness of 1.24 mm and a momentum thickness of 0.52 mm are observed for a flow velocity of 10 m/s, resulting in a form factor of 2.38, representing laminar inflow. With a tripping tape present at a flow speed of 30 m/s, a displacement thickness of 0.61 mm and a momentum thickness of 0.49 mm are obtained (form factor 1.25 and turbulent inflow). Furthermore, at a height of 5.4 mm, the velocity in the boundary layer equals 99% of the inflow velocity in that case.

The cylinder's height is more than 20 times the boundary-layer thickness δ_{99}. Therefore, the boundary layer is considered to be negligible and to have a minor influence on the flowfield [14]. Boundary-layer measurements are also performed during the runs in the aerodynamic wind tunnel using LDA. At an inflow velocity of 10 m/s, the inflow profile is measured at a distance of 5*D* upstream of the cylinder's center. A displacement thickness of 0.78 mm and a momentum thickness of 0.35 mm are observed (form factor 2.21) in that case.

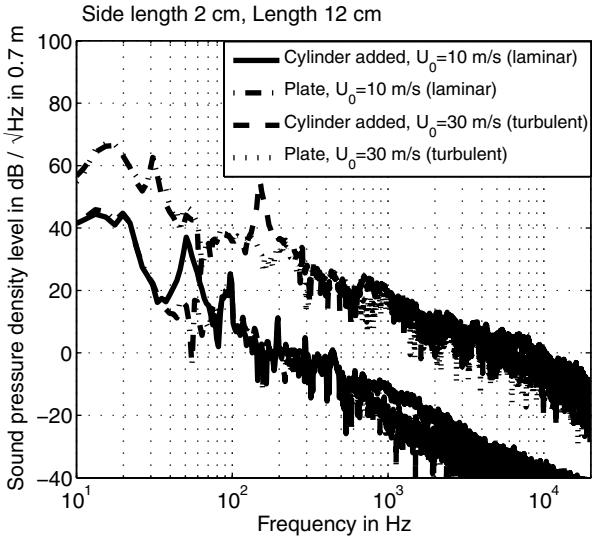

Fig. 9 Flow-induced sound of the reference-case square cylinder in the narrowband spectrum.

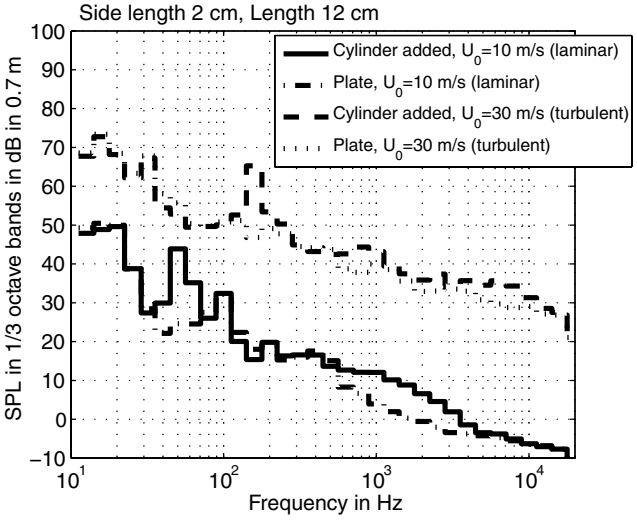

Fig. 10 Flow-induced sound of the reference-case square cylinder in one-third-octave bands.

III. Flow-Induced Sound of Cylinder Geometries

A. Sound Field of Square Cylinders in Crossflow at Different Reynolds Numbers

The acoustic field is generated at the frequency of the vortex shedding. The well-known aeolian tone can clearly be discerned at the vortex shedding frequency (see Figs. 9 and 10). At a flow speed of 10 m/s, a major frequency of 52 Hz (± 1 Hz) is observed, resulting in a Strouhal number St of 0.104 based on cylinder side length D. For turbulent inflow conditions at a speed of 30 m/s, the peak of the shedding frequency is located at 152 Hz ($St = 0.101$). Figure 9 displays the recorded sound pressure levels in one-third-octave bands.

Additional to aeolian tone, an increase in the broadband noise in the range of 500 to 10 kHz is observed. In this paper, the focus is directed mostly on the physics of the aeolian tone. For each velocity, the measurement is carried out twice to identify the active frequency range of the respective cylinder setup. First, the generated sound is recorded when the cylinder is present, and in the second step, the cylinder is removed and only the noise of both the wind tunnel and the remaining flat plate is obtained. In both cases, the cross spectrum between the two microphones (for their position, see Fig. 5) is evaluated to suppress uncorrelated noise. The respective signals are recorded simultaneously for 60 s with a sample rate of 44.1 kHz.

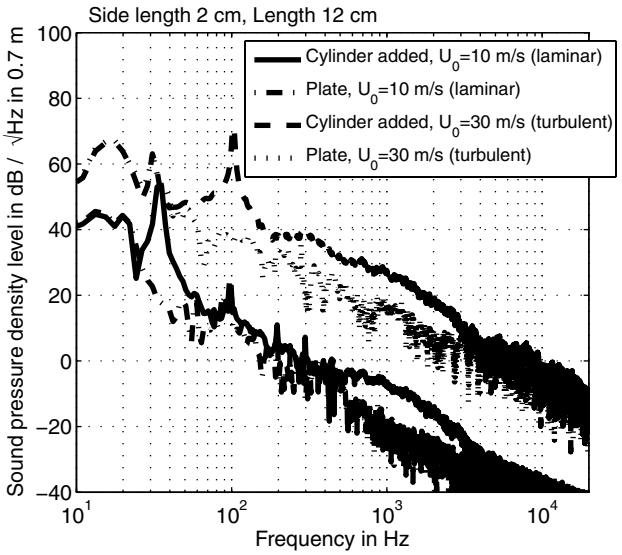

Fig. 11 Flow-induced sound of a square cylinder with an elliptical afterbody in the narrowband spectrum.

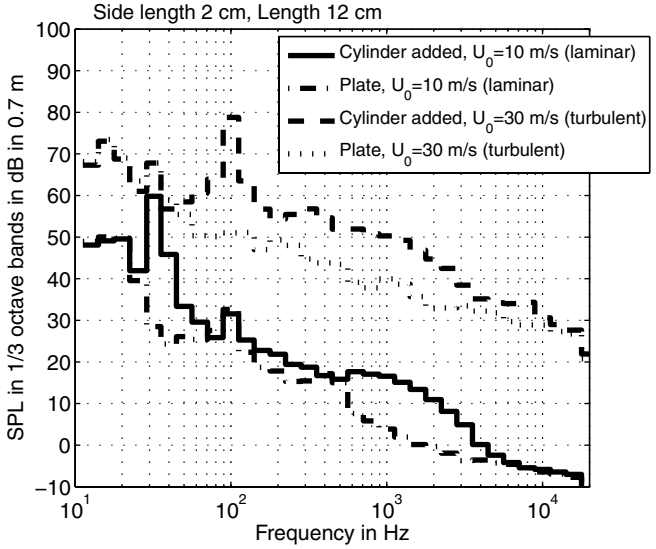

Fig. 12 Flow-induced sound of a square cylinder with an elliptical afterbody in one-third-octave bands.

These acoustic measurements are carried out with no obstructions other than the cylinder itself present in the flow.

Comparisons with published data are not feasible. The data presented by Sakamoto [13] for three-dimensional flow refer to a case in which the cylinder length is not more than twice the boundary-layer thickness δ_{99}. Although the aspect ratio is 6, as in the setup presented here, the cylinder length (120 mm) is more than 20 times larger than the boundary layer δ_{99} (5.4 mm). However, Strouhal numbers obtained in almost solely two-dimensional flow situations cannot be taken as a reference for this setup either, due to their difference in aspect ratios (i.e., $L/D = 15$ or 120 [8,10]) and the absence of wall and end effects due to different setups.

B. Sound Field of Square Cylinders with Modified Geometries

Variations in the cylinder's geometry, as shown in Fig. 4, lead to significant changes in the radiated sound field. Attaching an elliptical half-body in the recirculation area downstream of the cylinder reduces the pressure-based drag of the cylinder. The coefficient of drag c_D, obtained by evaluation of the flowfield via LDA, is reduced to $c_D = 0.9$, compared with $c_D = 1.9$ in the case of the unmodified cylinder. However, the flow-induced sound is intensified and the aeolian tone is shifted to lower frequencies ($f_{\text{shed}} = 36$ Hz $\pm$ 1 Hz) at $U_0 = 10$ m/s), resulting in a Strouhal number of 0.072 (see Figs. 11 and 12). The results also show a higher level of the broadband-noise spectrum in comparison with the reference geometry.

Using the wedge as an afterbody on the rear side of the cylinder also increases the radiated noise, as can be seen in Figs. 13 and 14. The major shedding frequency [in this case, $f_{\text{shed}} = 48$ Hz ($\pm$1 Hz), corresponding to a Strouhal number of 0.096] is only slightly changed, compared with the unmodified square cylinder. The broadband-noise level is similar to the results obtained for the test case with an elliptical afterbody.

Adding an elliptical half-body in front of the cylinder prevents the flow from separating at the leading edges of the square cylinder and thereby effectively reduces the pressure-based drag. For a laminar flow velocity of 10 m/s, only a slight increase in sound pressure is observed, making this setup the one with the least noise generated at this velocity. However, as can be observed in Figs. 15 and 16, little but significant noise is generated again when an inflow velocity of 30 m/s with a turbulent boundary layer is used. An equally small amount of noise as in the previous case is obtained when the short wedge is added in front of the cylinder. In this setup, little noise is generated for both velocities (see Figs. 17 and 18). The coefficient of drag is reduced to $c_D = 0.4$.

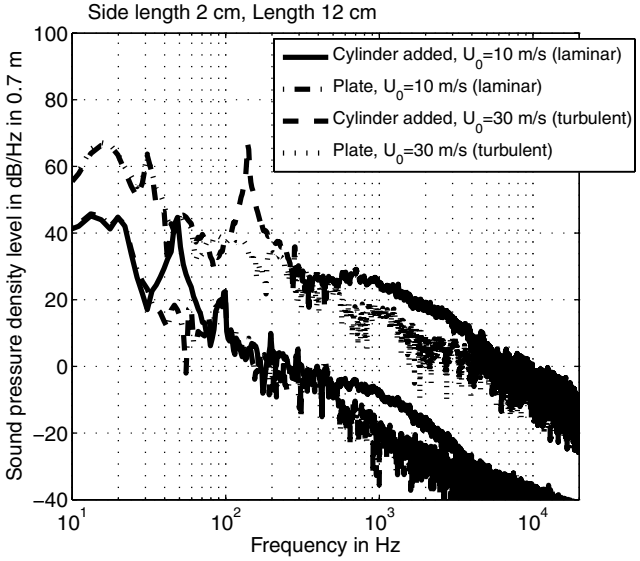

Fig. 13 Flow-induced sound of a square cylinder with an added wedge downstream in the narrowband spectrum.

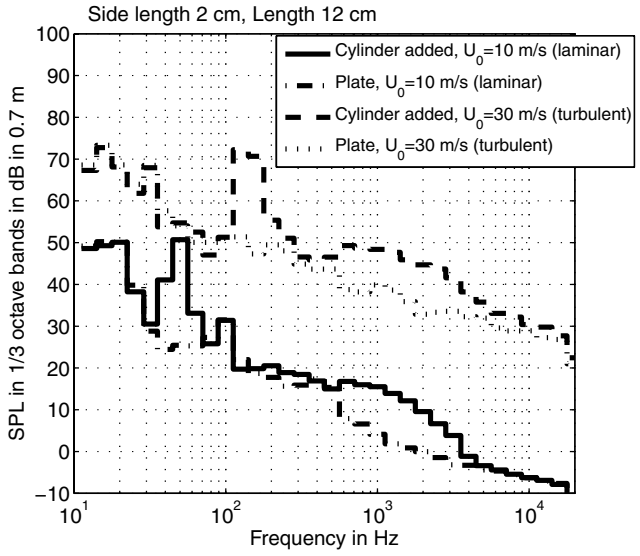

Fig. 14 Flow-induced sound of a square cylinder with an added wedge downstream in one-third-octave bands.

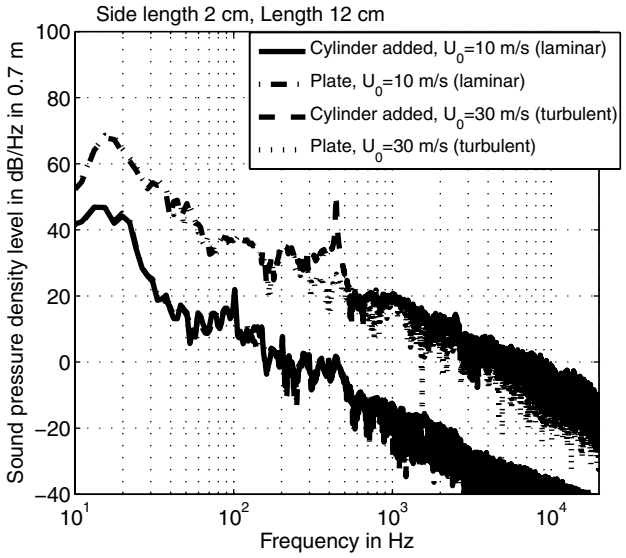

Fig. 15 Flow-induced sound of a square cylinder with an elliptical forebody in the narrowband spectrum.

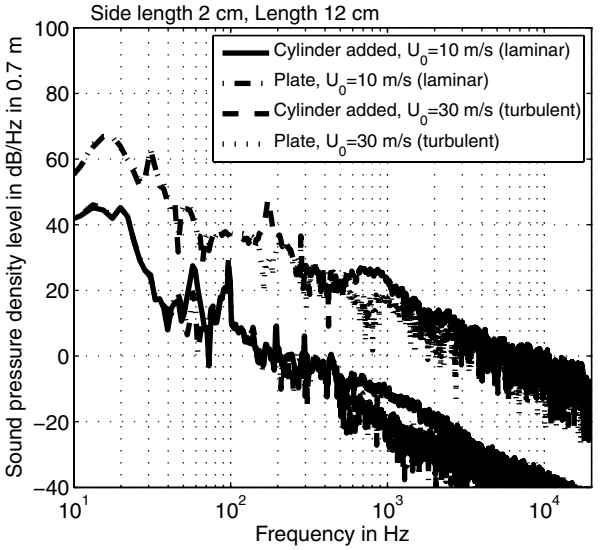

Fig. 17 Flow-induced sound of a square cylinder with a short wedge in front in the narrowband spectrum.

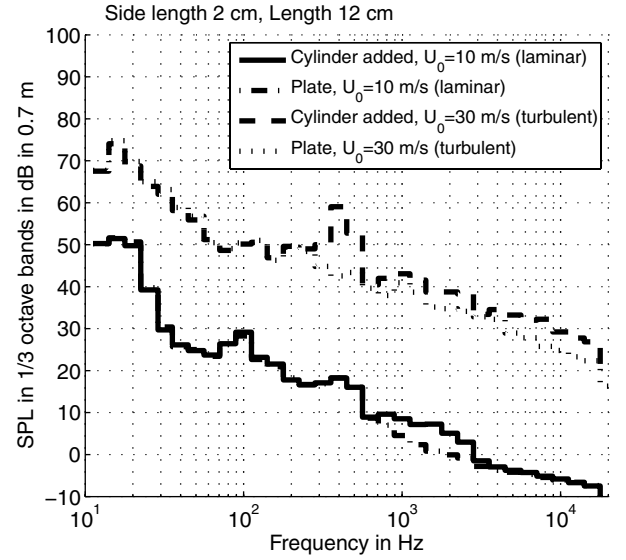

Fig. 16 Flow-induced sound of a square cylinder with an elliptical forebody in one-third-octave bands.

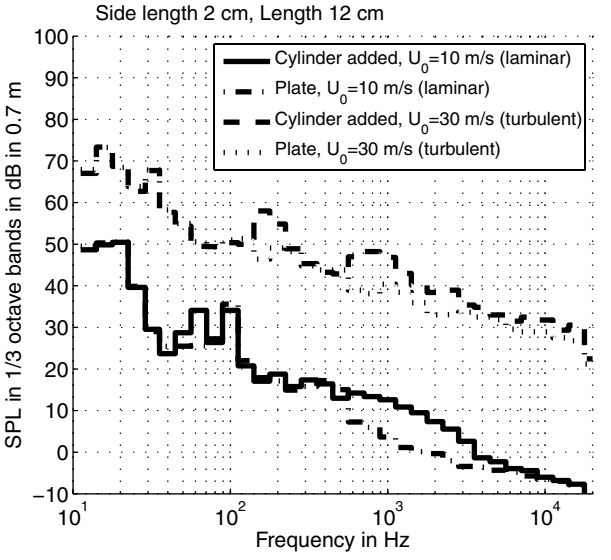

Fig. 18 Flow-induced sound of a square cylinder with a short wedge in front in one-third-octave bands.

Concerning the broadband noise, we can deduce that in the case of the elliptical forebody, a slight reduction is observed, whereas in the case of the wedge-shaped forebody, no significant change occurs, compared with the reference cylinder.

C. Comparisons

To facilitate the interpretation of the recorded sound pressure spectra, a ranking is created. First, the frequency of the respective aeolian tone is determined and the sound pressure levels around that tone are summed. The evaluation concentrates solely on the aeolian tone. Additional broadband contributions (e.g., as present in the case of an elliptical afterbody) are not taken into account.

The evaluation is carried out at a flow velocity of 30 m/s. Table 1 and Fig. 19 show that among the subset of geometries investigated here, all half-bodies that are added in front of the cylinder lead to a noise reduction, whereas all objects added downstream lead to an increase in noise, compared with the unmodified cylinder. Both forebodies create less noise to an equal extent. Despite the wedgelike shape and the separation at the leading edges of the cylinder, this geometry leads to the same noise reduction as in the case with an elliptical forebody, using less space than an elliptical half-body takes up.

Table 1 also lists the coefficient of drag for selected geometries. In comparison with the measured induced sound pressure levels, it can be observed that a reduction in overall turbulent kinetic energy does

Table 1 Total sound pressure level in the frequency range containing an aeolian tone ($U_0 = 30$ m/s) and coefficient of drag ($U_0 = 10$ m/s)

Geometry	Sound pressure level, dB	Frequency range, Hz	c_D
Elliptical afterbody	78.9	103 ± 20	0.9
Wedge downstream	74.4	139 ± 20	——
Square cylinder	65.3	152 ± 20	1.9
Elliptical forebody	58.9	441 ± 20	——
Wedge in front	58.9	174 ± 20	0.4

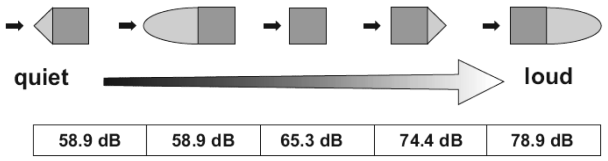

Fig. 19 Ranking of geometries: total sound-pressure-level frequency range containing an aeolian tone ($U_0 = 30$ m/s).

not necessarily also imply lower sound levels, as in the case of the square cylinder with an elliptical afterbody.

Having obtained these results, an investigation of the underlying fluid mechanical aspects responsible for these findings is started. For this purpose, three geometries are selected for further investigation. The connections between the observed sound fields and the flowfields are studied in the subsequent sections for the unmodified square cylinder, the cylinder with an elliptical afterbody, and the cylinder with a short wedge in front.

IV. Flowfield of Cylinder Geometries in Relation to the Radiated Sound Field

A. Mean Flowfield and Turbulent Quantities

The flowfield of these selected configurations is investigated via LDA and constant-temperature anemometer. Figure 20 illustrates the three-dimensional flowfield of the selected test cases. They show a visualization of the flow, the velocity, and the turbulent kinetic energy distribution in different planes. The horseshoe-vortex system in front of the cylinder is caused by the adverse pressure gradient of the stagnation point. The recirculation zone and the wake behind the cylinder are typical flow features of these cases. On the edges of the cylinder side faces, the flow separates.

The flow over the top of the cylinder shows a different behavior. For the unmodified cylinder, the flow separates at the top leading edge and does not reattach. In the case of the cylinder with an elliptical afterbody, the flow detaches and reattaches on the top. The flow over the cylinder with a wedge in front does not show a separation.

The coefficients of the drag calculated based on the momentum loss in comparison of the mean velocity distribution in different planes before and behind the cylinder are listed in Table 1. The results correlate with the amount of turbulent kinetic energy k in each respective test case. It corresponds to the magnitude of its individual drag coefficient. The highest amount of turbulent kinetic energy and the largest coefficient of drag are observed for the flow around the unmodified cylinder.

In the following, only some of the planes measured are used to describe the relation of characteristic flow phenomena to the radiated sound. The complete data set of the LDA measurements can be found elsewhere [23].

1. *Unmodified Square Cylinder*

The interpretation of the velocity and turbulence field is focused on a single plane behind the cylinder. Similar results can be found in other measurement planes. The y–z plane used for discussion is located two cylinder side lengths downstream of its rear side. Figure 21 displays the distribution of the mean velocity in that plane. Information about the distribution of the total turbulent kinetic energy can be found in Fig. 22. The velocity fluctuations are symmetric to the y–z plane, as can be seen in the vortex cores due to the periodic flow separation at the cylinder's leading edges. Fluctuations of the U and V components of the velocity are at about the same level and are larger than fluctuations of the third component W.

2. *Square Cylinder with an Elliptical Afterbody*

The distribution of the mean velocity and the turbulent kinetic energy in the same plane as for the unmodified square cylinder is shown in Figs. 23 and 24, respectively, for the case of the square cylinder with the elliptical afterbody. Overall turbulence is reduced compared with the unmodified square cylinder and the distribution is also symmetric to the y–z plane. However, in this case, velocity fluctuations are dominated by fluctuations of the U component, whereas the V and W fluctuations are at about the same level. The locations of flow separation remain the same as in the unmodified setup. However, flow that separates at the upper leading edge reattaches due to the added afterbody. Therefore, no roof vortex is present in the wake and the vortex street is not subject to its influence and can develop undisturbed.

3. *Square Cylinder with a Short Wedge Added in Front*

In that particular case, the fluctuations of all velocity components are of about the same magnitude. Furthermore, the flowfield (both mean and fluctuating field) is no longer symmetric to the y–z center plane (see Fig. 25) and no flow separation occurs at the upper leading edges of the wedge. A roof vortex of a slightly smaller size than in the reference geometry is nevertheless present in the cylinder's wake. Turbulence levels found downstream of the square cylinder with the wedge added in front are the lowest among the subset of geometries selected (see Fig. 26).

B. Dynamics of the Flowfield in Correlation with the Radiated Sound Field

To investigate the dynamic aspects of the respective flowfields, hot-wire measurements are carried out in the x–y plane at the position $z = L/2$, as shown in Fig. 5. The orientation of the wire is thereby perpendicular to the x–y plane. In the setup, fluid mechanical and acoustic measurements are undertaken simultaneously.

1. *Unmodified Square Cylinder*

The previous section demonstrated that the maximum of kinetic energy values are located in the shear layer between the outer flow and the recirculation zone behind the cylinder. The velocity spectrum in Fig. 27 corresponds to the location of the maximum of the kinetic energy (see Fig. 20). The vortex shedding frequency at an inflow velocity of 10 m/s is 52 Hz ($\pm$1 Hz) in this measurement. The selected measuring point is marked in Fig. 28, in which the rms values of the velocity fluctuations in the shedding-frequency range of 48–56 Hz are displayed. Knowing the basic frequency present in the flowfield, one can visualize the spatial distribution at that frequency. The highest values are located in the shear layer between $1D$ and $3D$ behind the cylinder. The separation at the leading edge is also clearly visible.

The coherence spectra between local flow velocity and generated sound show distinctive peaks only around the shedding frequency (see Fig. 29). The coherence spectrum in this case is evaluated at the same point ($x = 3D$, $y = 1D$, and $z = L/2$).

Because the position of the microphone remains fixed throughout the measurement and only the hot-wire probe is traversed, one can also use the data to characterize the coherence of the flowfield. Although the flowfield is sampled subsequently, the microphone signal serves as a reference signal that keeps its statistical properties constant; that is, if at a certain position (A) the local flow velocity is coherent to the radiated sound and at another position (B) a similar level of coherence is observed, one can conclude that the flowfield is also coherent at these two positions. The distribution of the coherence in Fig. 30 indicates that there are regions with a homogeneous distribution of coherence near the leading edge, which contains high coherence levels by small velocity fluctuations within the shedding-frequency range. Downstream of the cylinder in regions with large velocity fluctuations, we observe a less homogeneous distribution. We explain this behavior by a decreased coherence in the flowfield. Overall, the local velocity fluctuations are very coherent to the radiated sound in that frequency range.

2. *Square Cylinder with an Elliptical Afterbody*

In the case of the square cylinder with an elliptical afterbody, the large magnitudes of the velocity fluctuations at the shedding frequency as compared with the standard configuration (see Fig. 30) are in contrast to the smaller kinetic energy. The shedding frequency is at 36 Hz ($\pm$1 Hz), as observed previously in the acoustic

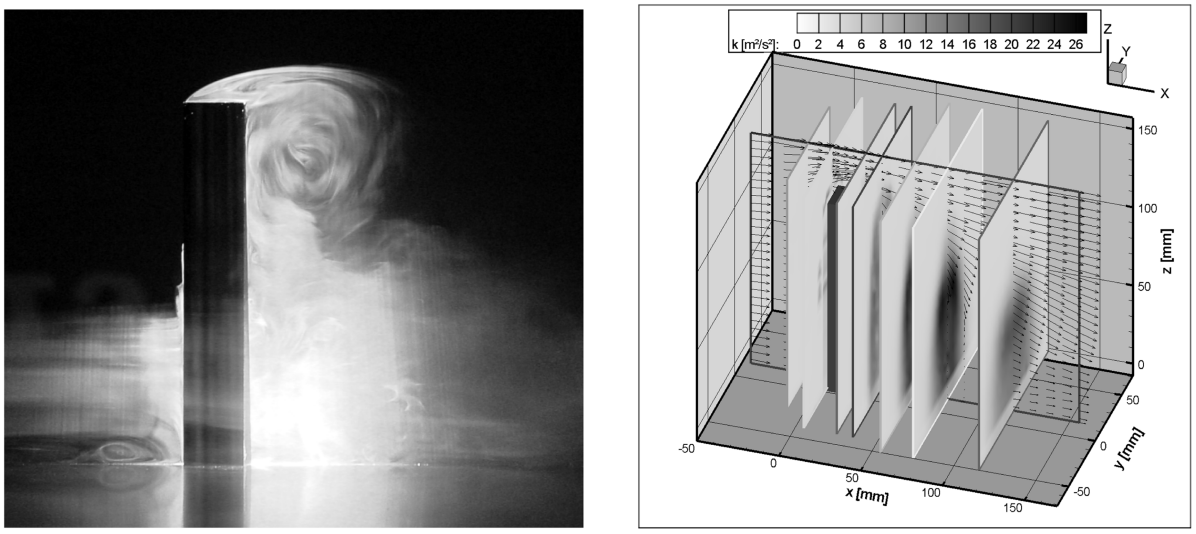

a)

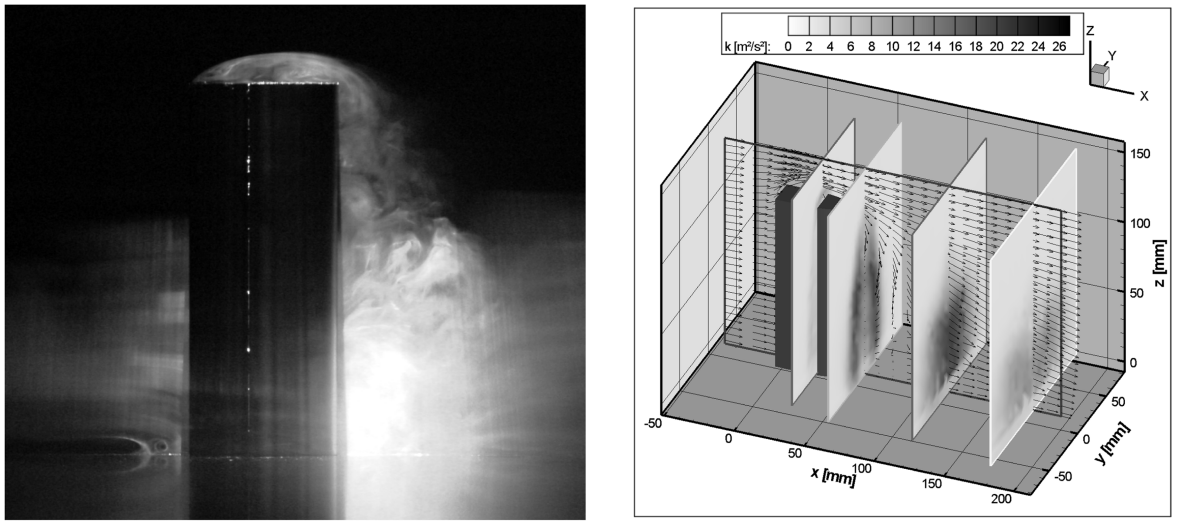

b)

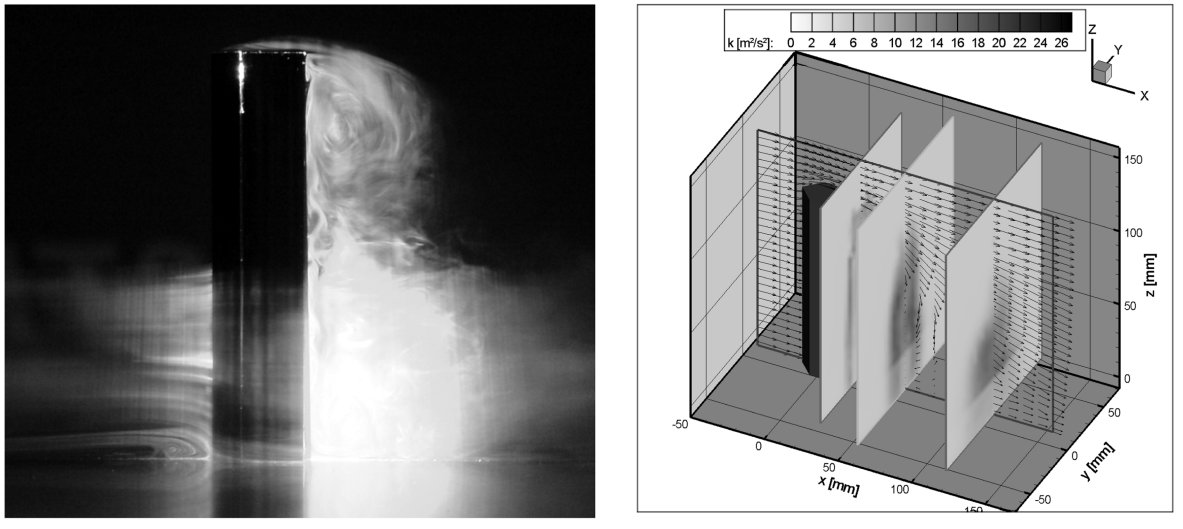

c)

Fig. 20 Flow visualization, velocity distribution, and turbulent kinetic energy for a) unmodified cylinder, b) cylinder with an elliptical afterbody, and c) cylinder with a wedge in front ($U_0 = 10$ m/s).

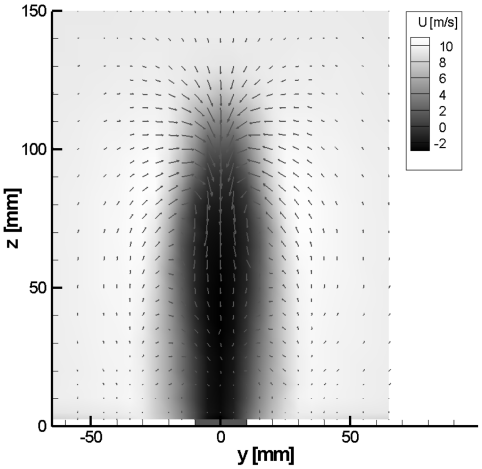

Fig. 21 Mean velocity in the streamwise direction of an unmodified square cylinder at $U_0 = 10$ m/s in the y–z plane.

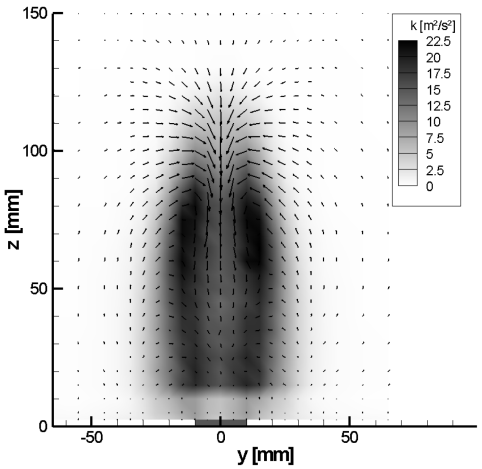

Fig. 22 Turbulent kinetic energy of an unmodified square cylinder at $U_0 = 10$ m/s in the y–z plane.

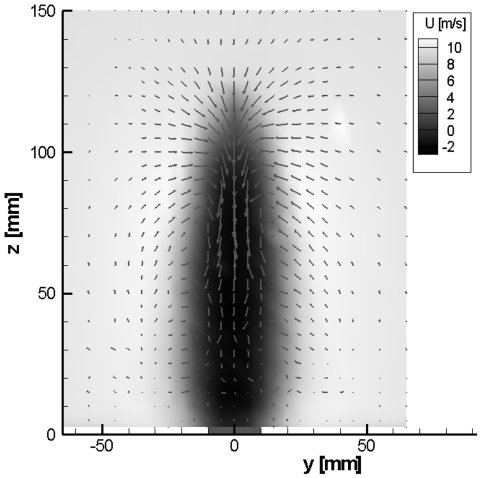

Fig. 23 Mean velocity in the streamwise direction of a square cylinder with an elliptical afterbody at $U_0 = 10$ m/s in the y–z plane.

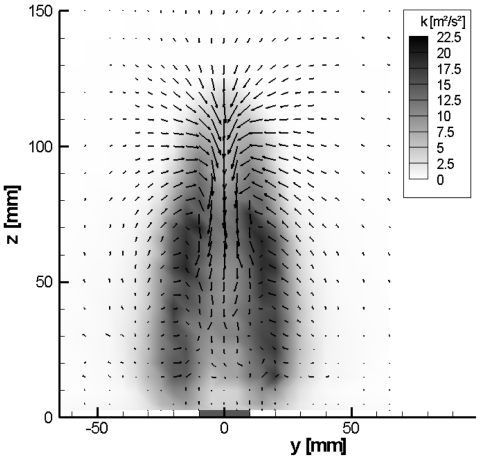

Fig. 24 Turbulent kinetic energy of a square cylinder with an elliptical afterbody at $U_0 = 10$ m/s in the y–z plane.

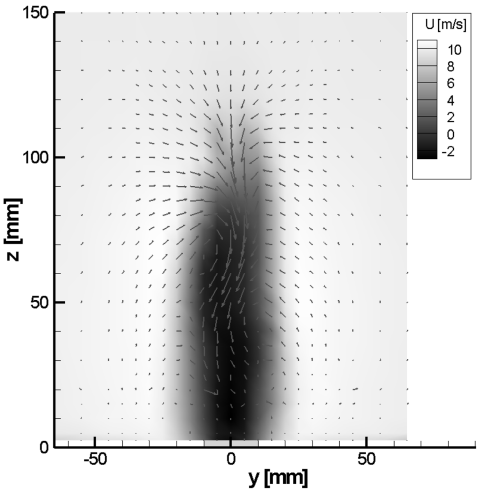

Fig. 25 Mean velocity in the streamwise direction of a square cylinder with a short leading wedge at $U_0 = 10$ m/s in the y–z plane.

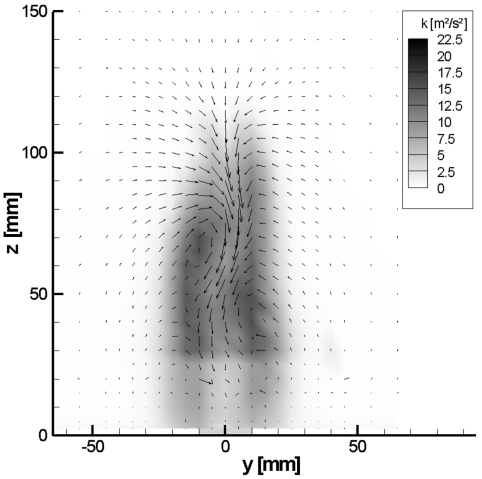

Fig. 26 Turbulent kinetic energy of a square cylinder with a short leading wedge at $U_0 = 10$ m/s in the y–z plane.

measurements. Figure 31 contains the velocity spectra at a point $1D$ downstream of the elliptical afterbody and $1D$ outside the centerline in the lateral direction. The point is chosen to correspond also to the location of the maximum of the rms values in the frequency range of 32–40 Hz. The respective location is marked in Fig. 32, which displays the velocity fluctuations. Separation again occurs at the leading edges.

With respect to the radiated sound field, the coherence levels are increased in the setup consisting of the square cylinder with the elliptical afterbody, as can be seen both in the local coherence

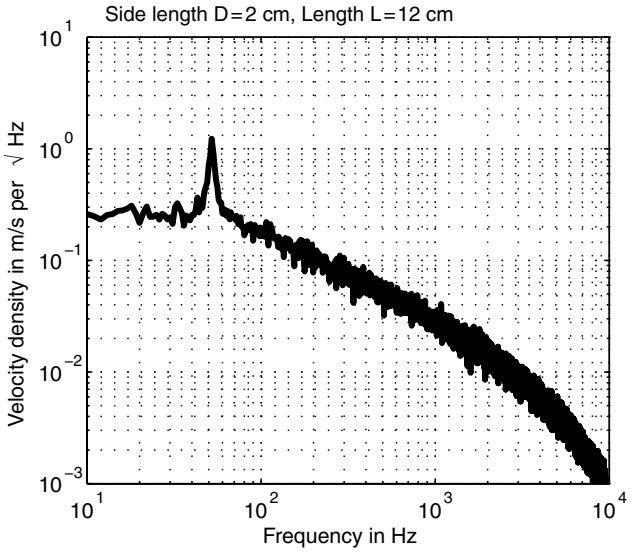

Fig. 27 Velocity spectrum at $(x, y) = (3D, 1D)$ of flow around a square cylinder ($U_0 = 10$ m/s); $D = 2$ cm and $L = 12$ cm.

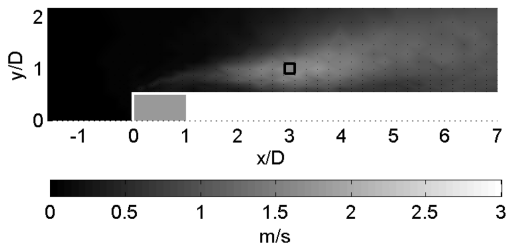

Fig. 28 Distribution of velocity fluctuations in the frequency range of 48–56 Hz in the y–z plane at $z = L/2$ and $U_0 = 10$ m/s (unmodified square cylinder).

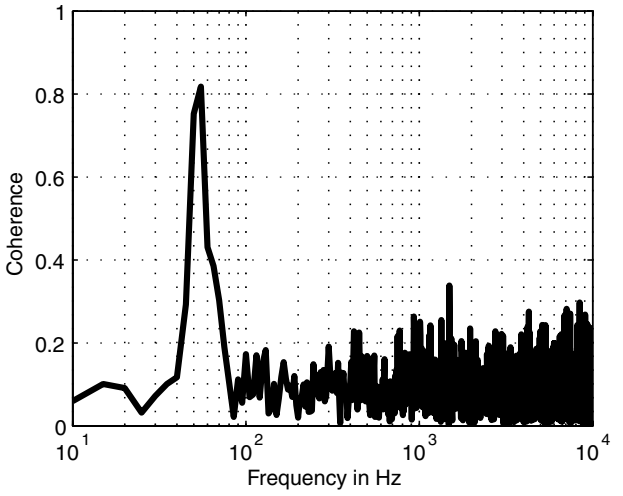

Fig. 29 Coherence spectrum between local velocity and radiated sound at $(x, y) = (3D, 1D)$; unmodified square cylinder ($U_0 = 10$ m/s).

spectrum (see Fig. 33) and in the spatial distribution of the coherence in the frequency range around the vortex shedding frequency (see Fig. 34). Medium levels of coherence are only present in regions close to the surface of the cylinder and its afterbody downstream of the leading-edge separation.

Additionally, the coherence is distributed very homogeneously throughout the observed region, which can be interpreted as the flowfield being very coherent within itself (in the respective frequency range used in Fig. 34).

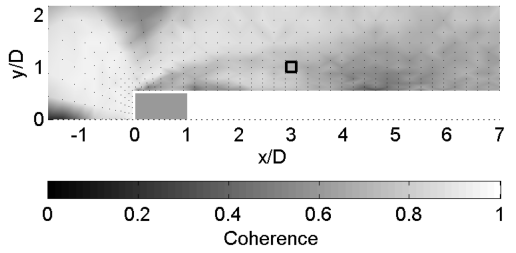

Fig. 30 Distribution of coherence between local flow velocity and radiated sound in the frequency range of 48–56 Hz in the x–y plane at $z = L/2$ and $U_0 = 10$ m/s (unmodified square cylinder).

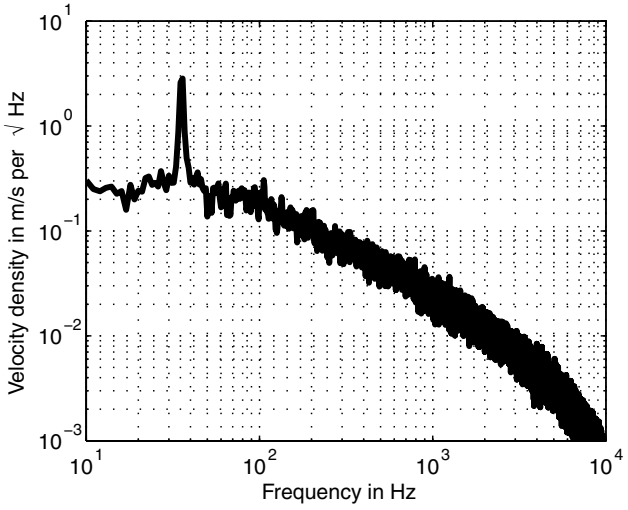

Fig. 31 Velocity spectrum at $(x, y) = (1D, 1D)$ of flow around a square cylinder with an elliptical afterbody ($U_0 = 10$ m/s).

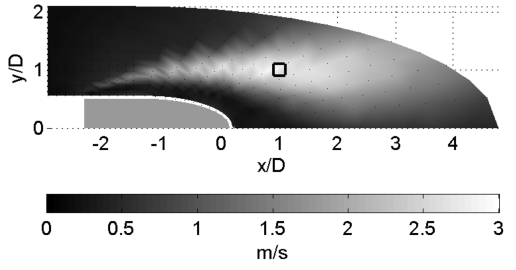

Fig. 32 Distribution of velocity fluctuations in the frequency range of 32–40 Hz in the x–y plane at $z = L/2$ and $U_0 = 10$ m/s (square cylinder with an elliptical afterbody).

3. Square Cylinder with a Short Wedge Added in Front

Placing the short wedge in front of the square cylinder causes the flow to separate at the interfacing corner between these two geometries. The magnitude of the shedding frequency is lower than in both previous cases (see Fig. 35). A peak frequency of 60 Hz (±1 Hz) is observed. The location of the point used to display the velocity spectrum is shown in Fig. 36, in which the spatial distribution of velocity fluctuations in the frequency range of 56–64 Hz is displayed.

Less distinctive levels of coherence are found in this case than in the two other configurations. The local coherence evaluated in a region with maximum velocity fluctuations again shows the predominant peak around the shedding frequency (see Fig. 37). However, coherence levels are lower throughout the scanned area, as shown in Fig. 38 for the frequency range of 56–64 Hz. Furthermore, the distribution of the coherence is very inhomogeneous.

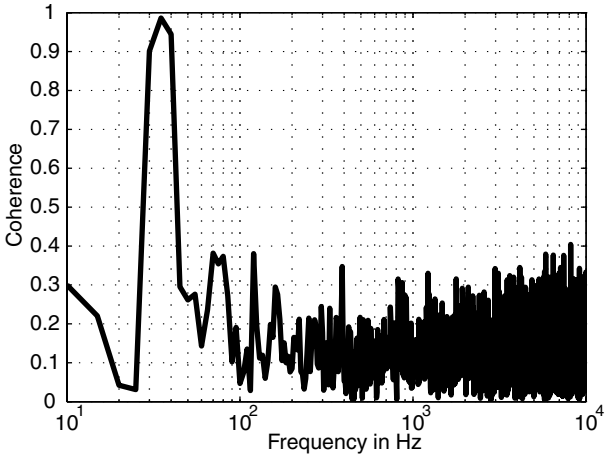

Fig. 33 Coherence spectrum between local velocity and radiated sound at $(x, y) = (1D, 1D)$ and $U_0 = 10$ m/s (square cylinder with an elliptical afterbody).

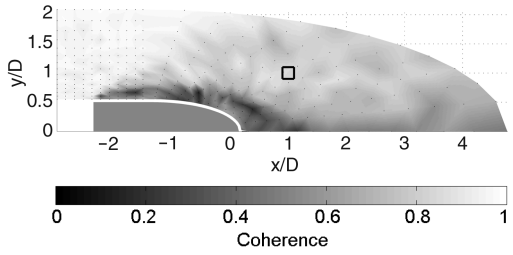

Fig. 34 Distribution of coherence between local flow velocity and radiated sound in the frequency range of 32–40 Hz in the x–y plane at $z = L/2$ and $U_0 = 10$ m/s (square cylinder with an elliptical afterbody).

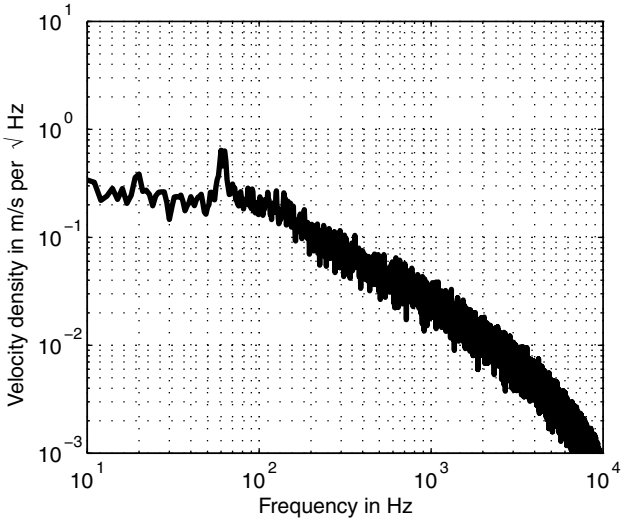

Fig. 35 Velocity spectrum of flow around a square cylinder with a short wedge in front at $(x, y) = (4.6D, 0.7D)$ and $U_0 = 10$ m/s.

C. Distribution of Wall Pressure

Because of the three-dimensional flowfield around the square cylinder, the distribution of the wall pressure along the cylinder's axis is not expected to be homogeneous. Therefore, local wall pressure is measured at the positions indicated in Fig. 39.

The shedding frequency is also clearly visible in the narrowband spectra of the wall pressure recorded in the center of the cylinder face used for pressure measurements (see Fig. 40). Because of conservation of momentum, the fluctuating flowfield around the cylinder induces fluctuations of the wall pressure. Pressure levels of

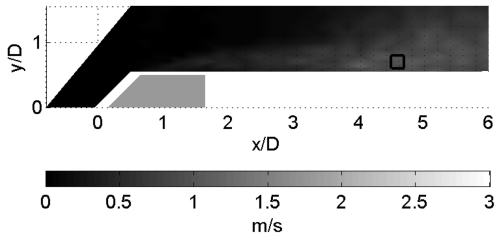

Fig. 36 Distribution of velocity fluctuations in the frequency range 56–64 Hz in the x–y plane at $z = L/2$ and $U_0 = 10$ m/s (square cylinder with a short wedge in front).

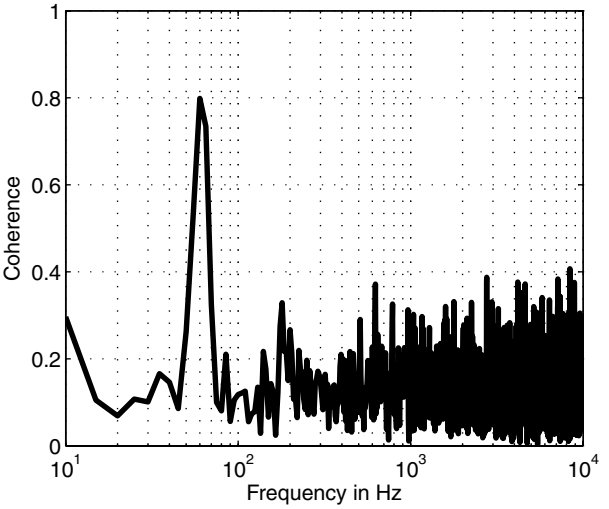

Fig. 37 Coherence spectrum between local velocity and radiated sound at $(x, y) = (4.6D, 0.7D)$ and $U_0 = 10$ m/s (square cylinder with a short wedge in front).

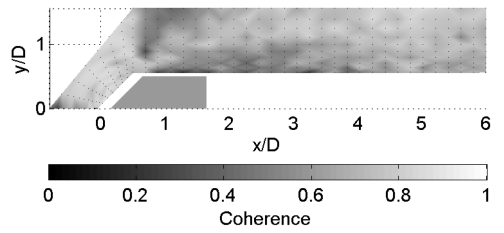

Fig. 38 Distribution of coherence between local flow velocity and radiated sound in the frequency range 56–64 Hz in the x–y plane at $z = L/2$ abd $U_0 = 10$ m/s (square cylinder with a short wedge in front).

105–120 dB (relative to 20 μPa) in one-third-octave bands are observed in the case of an unmodified square cylinder for respective flow velocities of $U_0 = 10$ and 30 m/s.

The coherence between local wall pressure (measured at position 4 in Fig. 39) and radiated sound is displayed in Fig. 41. The induced sound is recorded 0.7 m away from the cylinder, leading to a run time of about 2 ms between the sensors. Before calculation of the coherence spectrum, the run-time difference is compensated. The coherence is very significant around the shedding frequency. Additional medium levels of coherence can be observed at higher frequencies. The coherence resulting from a deliberate decorrelation of the signals is also plotted in Fig. 41, thus providing a lower limit for the coherence [24].

To determine the phase difference between measurement positions displayed in Fig. 5, the signal of a wall-pressure probe in position A is recorded simultaneously with the signal of a microphone located 0.7 m away from the cylinder. In a following step, the cylinder is rotated and the measurement is repeated for the wall-pressure probe in position B. Thereby, the phase difference between the microphone and pressure probe is compensated and only

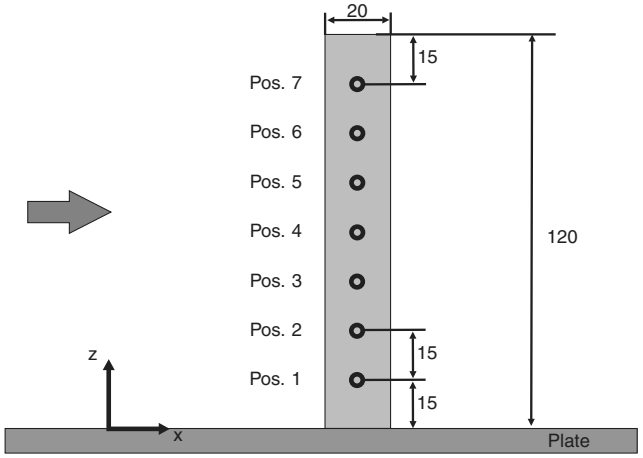

Fig. 39 Measurement positions of local wall pressure (distances in millimeters).

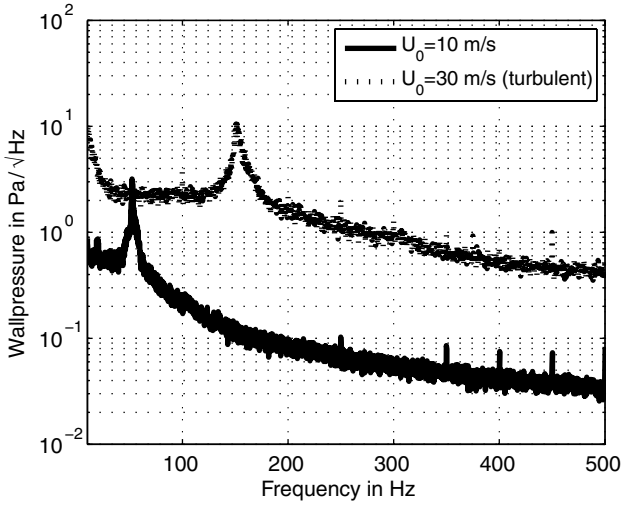

Fig. 40 Wall pressure spectra in the center of the side face normal to flow (unmodified square cylinder); $D = 2$ cm.

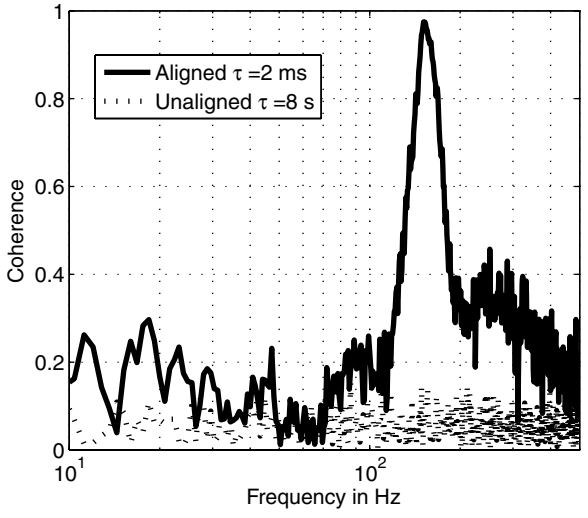

Fig. 41 Coherence between local wall pressure and radiated sound for an unmodified square cylinder at $U_0 = 30$ m/s.

the phase difference between wall pressures in positions A and B is evaluated. As can be seen in Fig. 42, for an inflow velocity of 30 m/s, the phase difference between opposing cylinder sides not incident to the flow is close to 180 deg, indicating opposite phases and dipolelike behavior. A phase difference of about 185 deg around the shedding frequency is also found when evaluating the phase of the cross spectrum between the two opposed microphones in Fig. 5.

To investigate the dipolelike behavior of the wall pressure and the radiated sound recorded on opposed locations, measurements of the directivity of the flow-induced sound intensity are carried out. Here, the active part of the sound intensity is analyzed and obtained at different positions, depicted in Fig. 43.

The normalized distribution of the flow-induced sound intensity of the square cylinder is shown in Fig. 44 for inflow velocities of 10 and 30 m/s. Both directivities are shifted slightly toward the direction of the approaching flow. For comparison, the ideal dipole characteristic of the induced sound of a circular cylinder at low Reynolds numbers is included. The obtained directivity of the sound radiation is in accordance with the theory of vortex sound. In [1], the vortex sound is discussed in detail, and by applying the theory of Powell, it has been shown that the direction of the radiated sound is determined by the cross product of the vorticity $\boldsymbol{\omega}$ and the velocity $\boldsymbol{U}$.

Figure 45 illustrates the case of the flow around a circular cylinder. Here, the plane spanned by the vortex lines are parallel to the x–z plane. The maximum of the sound radiation is located in the direction of the surface normal. However, in the case of a rectangular cylinder, the local velocity vector is different in the region of vortex separation. This results in an incline of the planes that are spanned from the

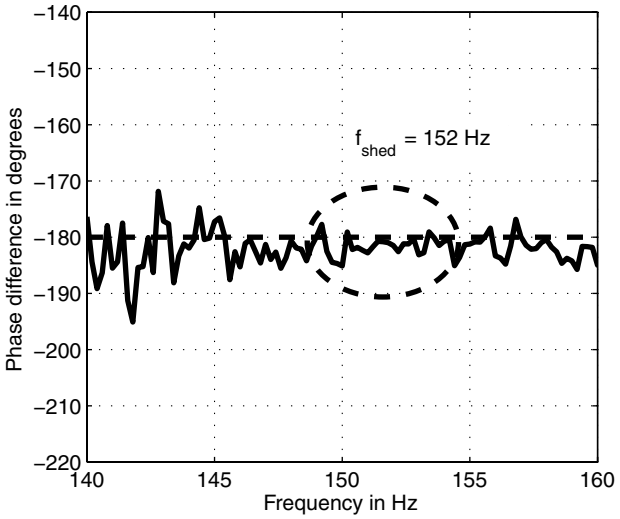

Fig. 42 Phase difference of wall pressures on opposed sides (unmodified square cylinder); $D = 2$ cm.

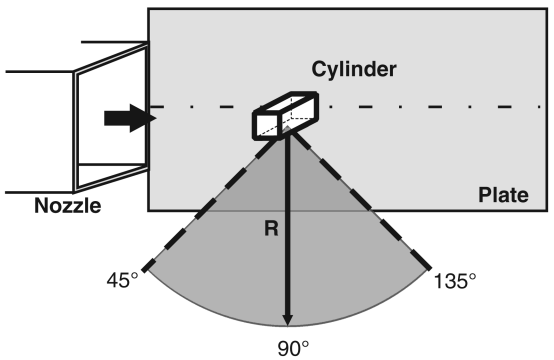

Fig. 43 Measurement positions used to determine the directivity of the radiated sound.

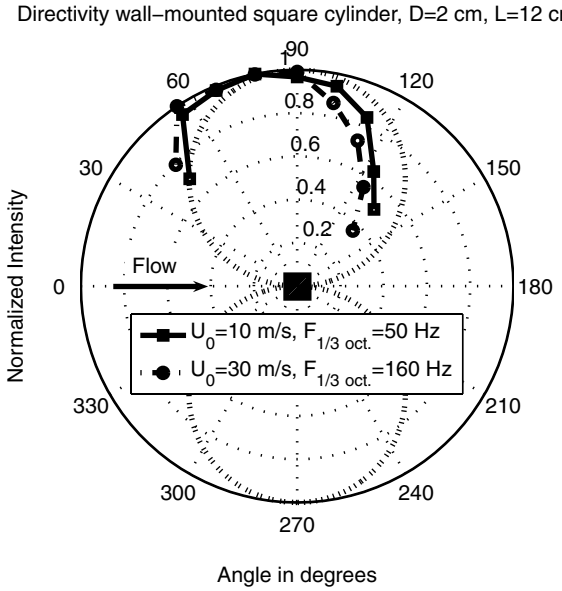

Fig. 44 Directivity of active part of flow-induced sound intensity of an unmodified square cylinder.

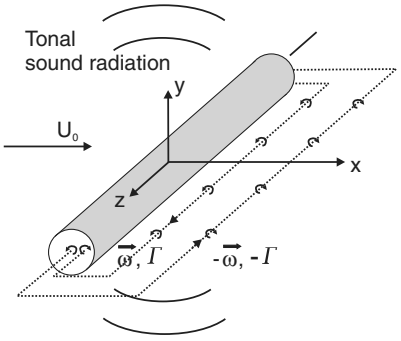

Fig. 45 Vortex structure and sound production on a circular cylinder [1].

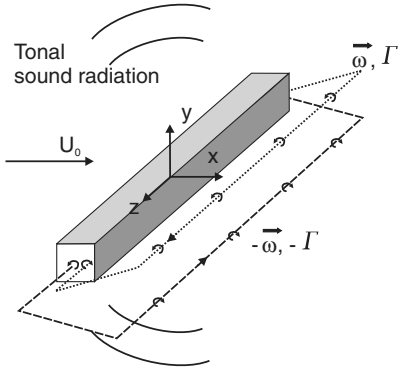

Fig. 46 Vortex structure and sound production on a rectangular cylinder.

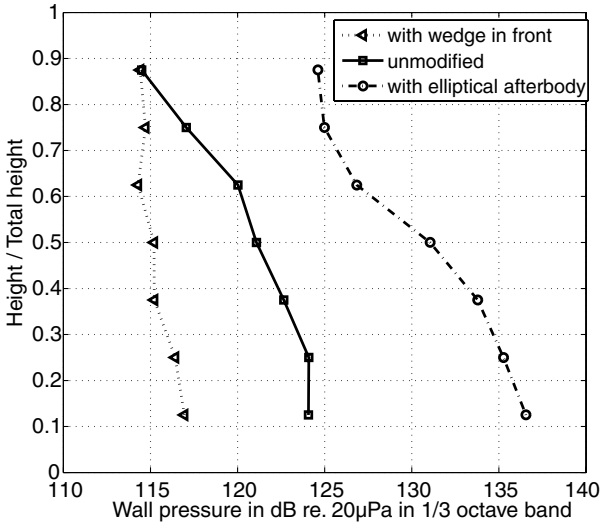

Fig. 47 Axial distribution of wall pressure in the one-third-octave band of shedding frequency.

vortex lines (see Fig. 46). As a consequence, the directivities are shifted slightly toward the direction of the approaching flow.

The axial distribution of the magnitude of wall-pressure fluctuations in the respective one-third-octave band of the shedding frequency is depicted in Fig. 47 for the selected geometry variations. The pressure fluctuations are not equally distributed. Close to the base of the cylinder, fluctuations are, on average, 8–10 dB larger than near the cylinder's top.

Furthermore, the fluctuation levels of the square cylinder with the elliptical afterbody throughout are higher than the pressure fluctuations observed on the unmodified square cylinder or the cylinder with the wedge in front. The latter case exhibits the lowest levels of fluctuation. In this case, the ranking of the radiated sound fields is mirrored in the wall-pressure fluctuations.

The flow separation at the leading edges of the square cylinder does not occur simultaneously along the cylinder's length [25]. This is of importance for the flow-induced sound, because phase differences of the flow separation lead to equivalent differences in sound radiation. The coherence length is used as a parameter to indicate the size of regions in which the separation can be considered to be occurring simultaneously. The correlation length is determined via evaluation of the correlation coefficient of wall-pressure signals simultaneously recorded at different positions. One probe is fixed at position 1, indicated in Fig. 39, whereas the position of the second probe is varied (positions 2–7). The analysis is carried out solely for the frequency range around the respective shedding frequency. Therefore, signals are bandpass-filtered around that frequency before evaluation.

The axial distribution of the correlation coefficients thereby obtained is shown in Fig. 48. The correlation coefficients decay with increasing distance between the probes. However, the correlation length of the square cylinder with the wedge in front is shorter than in the case of the square cylinder with the elliptical half-body. This effect clearly demonstrates that a short correlation length corresponds to a reduction in flow-induced sound.

D. Summary of the Correlation of the Flowfield to Radiated Sound

The results of the investigated geometry variations indicate that a reduction in kinetic energy does not necessarily also lead to a decrease in the level of radiated noise. The turbulent kinetic energy k is one of the basic physical quantities to predict noise in turbulent flows by using the stochastic noise generation and radiation model (e.g., [26,27]). The stochastic noise generation and radiation model will be used to determine, for example, broadband airframe noise. In our applications, the radiated sound field contains a low-frequency part that corresponds to the aeolian tone and a higher-frequency broadband-noise region. For all geometry variations, the obstacles are acoustically compact within the aeolian-tone frequency range. Hence, the dimensions of the cylinder are smaller than the acoustic wavelength. For the scattering of aerodynamic noise, some analogies exist with sound generation around trailing-edge noise [28,29], but it is very important to mention again that the investigated geometries are three-dimensional. They are wall-mounted on one side with a finite length L. In contrast, the trailing-edge investigations were done for two-dimensional geometries [1,20]. Nevertheless, one can profit from the physical expertise obtained with trailing-edge noise [20,28,29] to interpret the present aeroacoustic phenomena.

The mechanisms of sound generation for our investigations can be classified into four different cases, as displayed in Fig. 49. Case A

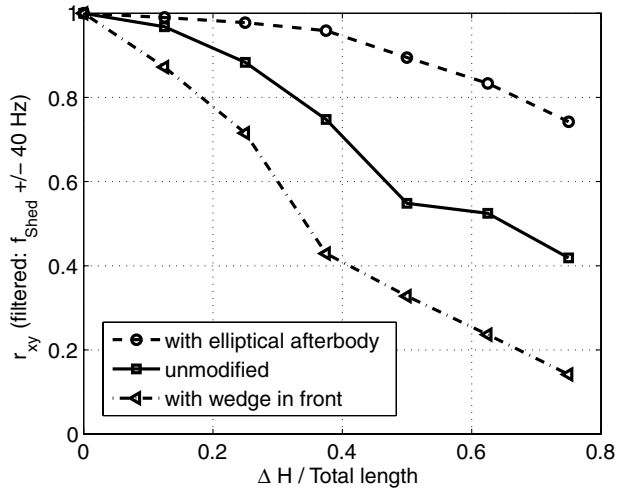

Fig. 48 Axial correlation of wall pressure along the cylinder's axis.

shows the flow around the unmodified cylinder. The flow separates at the front edge of the cylinder and generates a vortex street behind the cylinder. The instantaneous pressure distribution around the cylinder yields periodical lift and drag forces around the cylinder. The result is the characteristic low-frequency aeolian tone in the radiated sound field that corresponds directly to the shedding frequency. Similar behavior can be observed for trailing-edge noise problems (e.g., [30]).

For the cylinder with additional afterbody (case B), the flow separation point is also located on the front edge. Based on the extended dimension with an afterbody (wedge or half-ellipse), the size D_B of vortex-street formation is larger in comparison with the unmodified cylinder. However, the momentum loss is smaller, and so the resulting drag coefficient must be lower (see Table 1). The shift of the shedding frequency to a lower value can also be explained by the size of the separated flow region and by using similarity laws. The larger vortex structure must result in a lower shedding frequency. Furthermore, we detect the largest velocity fluctuations for this setup (see Fig. 32). However, it has to borne in mind that the magnitude of the velocity fluctuations alone cannot successfully be used as a factor in determining the level of flow-induced sound. Very important here is the influence of the roof vortex on the flow behind the cylinder. For the cylinder with an elliptical afterbody, it shows a reattachment of the flow, in contrast to the unmodified cylinder. Hence, the interaction of the roof vortex with the vortex street from side walls is stronger for the unmodified cylinder than for the case with an afterbody. The influence is also clearly visible in the coherence of the wall-pressure fluctuations. In case B, there is the highest coherence along the cylinder length L. The two-dimensionality of the vortex street is more developed. Hence, the result yields higher aeolian-tone generation. The broadband-noise level is also moderately higher. The reason for this increase can be explained by the interaction of the developed turbulent boundary behind the separation points with the shape of the trailing edge (e.g., [28]) of the modified cylinder.

Case C demonstrates the flow situation with an additional elliptical body in front. The separation point moves to the rear of the cylinder. The size of the recirculation zone is limited by the dimension D of the cylinder. Hence, the vortex shedding frequency and, subsequently, the frequency of the corresponding aeolian tone are increased and become the highest one for all investigated geometries. In the broadband spectrum, we observe only a small increase in the noise level, because the boundary layer around the cylinder is small.

The smallest aeolian-tone noise level will be reached with a sharp wedge in front of the cylinder, as displayed in Fig. 49 for case D. The separation point again moves to the leading edge. Hence, the size of the separation area is larger in case C, which results in a smaller tonal frequency. However, the value is still higher than in cases A and B, because the additional wedge forms a smaller separation size. The reason for the smallest tonal sound level lies in the suppression of the vortex street. The velocity distribution is no longer symmetrical in the y–z center plane (see Fig. 25). The sharp edge of the wedge is

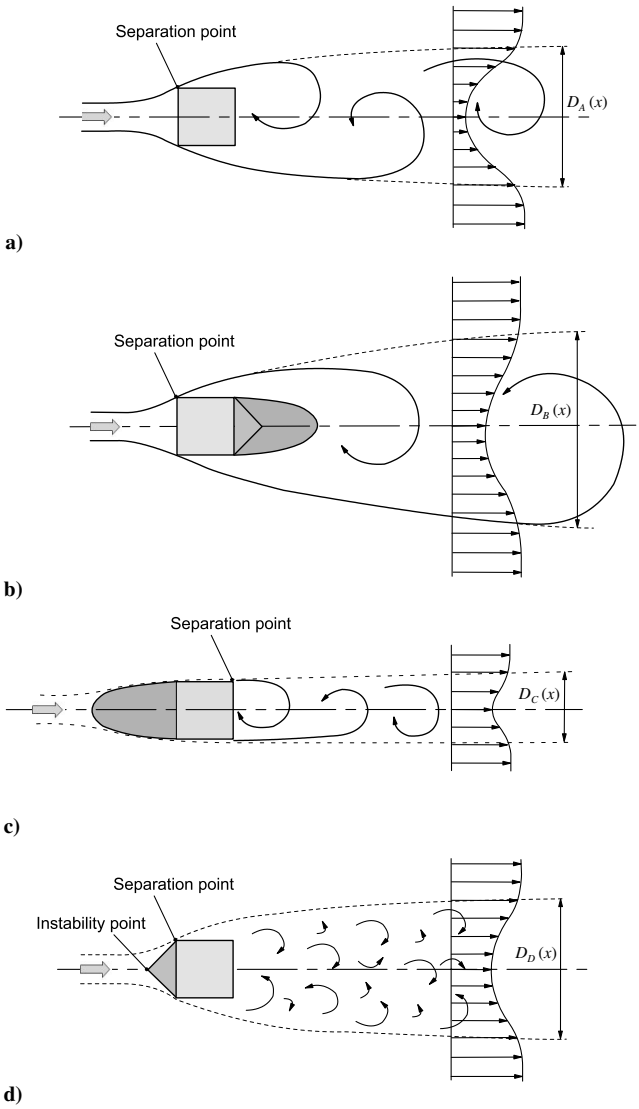

Fig. 49 Schematic flowfield of the investigated geometry variations: a) unmodified square cylinder, b) cylinder with an elliptical or wedge-shaped afterbody, c) cylinder with an elliptical forebody, and d) cylinder with a wedge in front.

responsible for this flow characteristic. The edge produces an instability point in front of the cylinder. It is usual that the oncoming flow in wind-tunnel experiments cannot be perfectly homogeneous and symmetrical with respect to the y–z center plane of the cylinder. Hence, small disturbances and inhomogeneities for such an instability point or line lead to nonuniform incoherent vortex formation. An additional identification of this flow behavior is visible in the relatively small coherence of the pressure fluctuations along the cylinder length L. An analysis [31] of the turbulence anisotropy behind the cylinder indicates a nearly isotropic turbulence status. With respect to the broadband-noise generation, the mechanism is similar to that for the unmodified cylinder. The eddies of the turbulent boundary layer on the cylinder sides interact with the back side of the cylinder and produce a turbulent shear layer behind the cylinder.

It can be summarized that drag reduction does not necessarily lead to noise reduction. Therefore, the criteria of the total turbulent kinetic energy k can only be used restrictively to estimate the sound generation. It is important to separate the noise spectrum in the aeolian-tone frequency and in the broadband-noise range. A reduction in the aeolian tone can be achieved by suppressing the two-dimensional vortex street around the side walls of the cylinder. The vortex formation is strongly affected by vortex separation on the roof of the cylinder and the geometric shape in front of the cylinder.

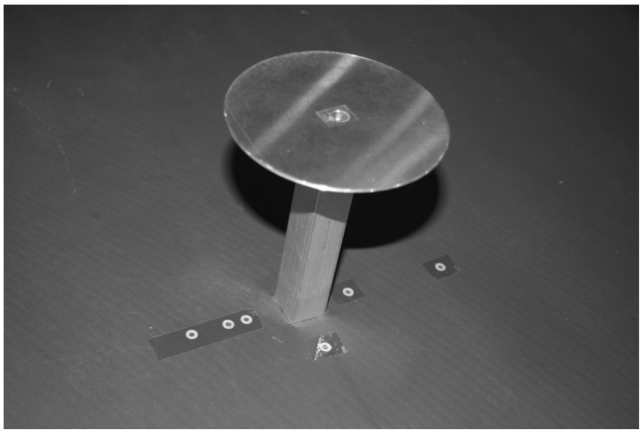

Fig. 50 Wall-mounted square cylinder with a circular end plate.

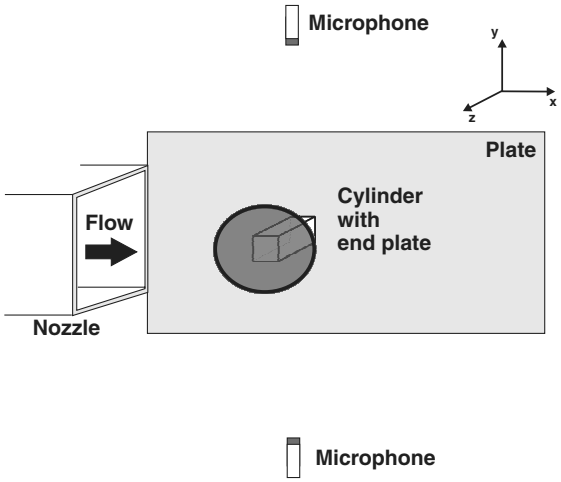

Fig. 51 Measurement setup consisting of a wall-mounted square cylinder with a circular end plate (not to scale).

V. Influence of the Roof Vortex on the Vortex Street and Induced Sound

In the previous sections, much emphasis was placed on the roof vortex and its influence on both the vortex street and the flow-induced sound. Therefore, additional measurements are carried out to underscore its dominating influence.

For this purpose, sound pressure measurements are repeated for selected geometries using a circular end plate [diameter of 100 mm (i.e., $5D$) and thickness of 1 mm] to suppress the development of the roof vortex (see Fig. 50). The same measurement setup as in the previous investigations is used (Fig. 51).

A. Unmodified Square Cylinder

Figure 52 displays the significant influence that the roof vortex has on the resulting sound pressure level. Eliminating the roof vortex increases the overall sound pressure level and especially the magnitude of the aeolian tone. It is increased by more than 23 dB

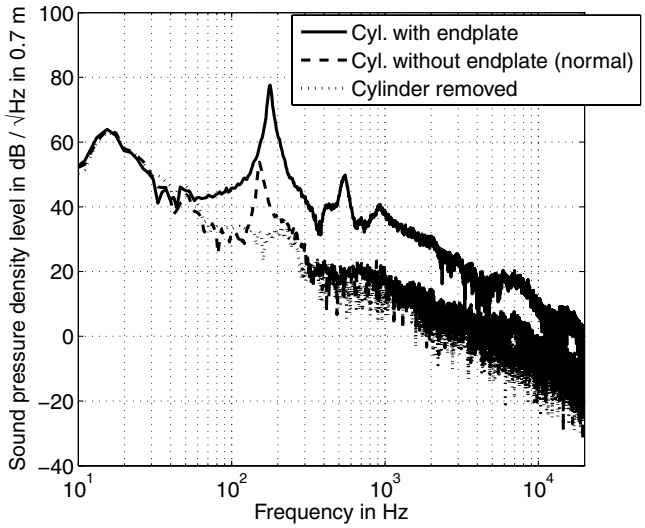

Fig. 52 Influence of the end plate on flow-induced sound of a wall-mounted square cylinder at $U_0 = 30$ m/s in the narrowband spectrum.

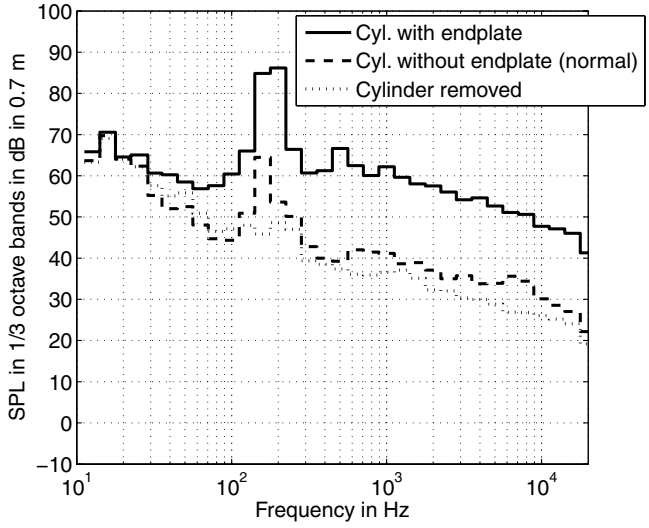

Fig. 53 Influence of the end plate on flow-induced sound of a wall-mounted square cylinder at $U_0 = 30$ m/s in one-third-octave bands.

when the roof vortex is suppressed (see Fig. 53 and Table 2). Additionally, the frequency of the aeolian tone shifts from 152 to 177 Hz, which demonstrates the influence of the roof vortex on the development of the vortex street.

B. Square Cylinder with an Elliptical Afterbody

As mentioned before, it is argued that in the configuration consisting of a square cylinder with an elliptical afterbody, the roof vortex is of less importance for the development of the vortex street because flow that separates at the leading edge at the top reattaches at the cylinder's afterbody and thereby does not disturb the vortex street. Following this argument, it can be observed in Figs. 54 and 55

Table 2 Comparison of flow-induced sound pressure levels of individual configurations and influence of the end plate at $U_0 = 30$ m/s in a frequency range around the respective aeolian tone

Configuration	Sound pressure level without end plate, dB	Frequency range, Hz	Sound pressure level with end plate, dB	Frequency range, Hz	Difference, dB
Cylinder with an elliptical afterbody	78.9	103 ± 20	85.5	98 ± 20	+6.6
Square cylinder	65.3	152 ± 20	88.6	177 ± 20	+23.3
Cylinder with a wedge in front	58.9	174 ± 20	73.4	211 ± 20	+14.5

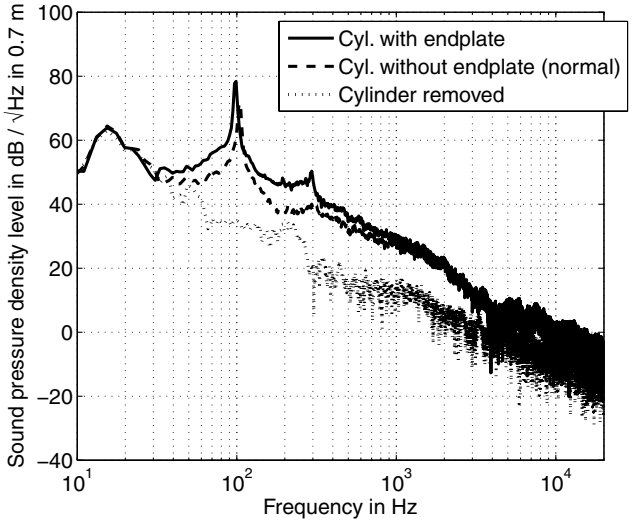

Fig. 54 Influence of the end plate on flow-induced sound of a wall-mounted square cylinder with an elliptical afterbody at $U_0 = 30$ m/s in the narrowband spectrum.

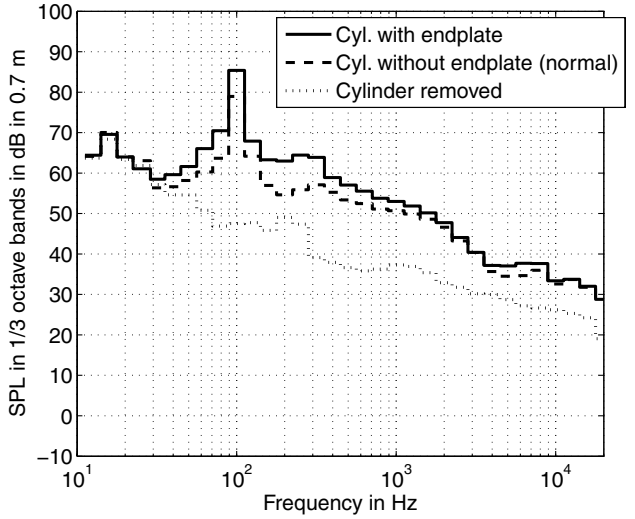

Fig. 55 Influence of the end plate on flow-induced sound of a wall-mounted square cylinder with an elliptical afterbody at $U_0 = 30$ m/s in one-third-octave bands.

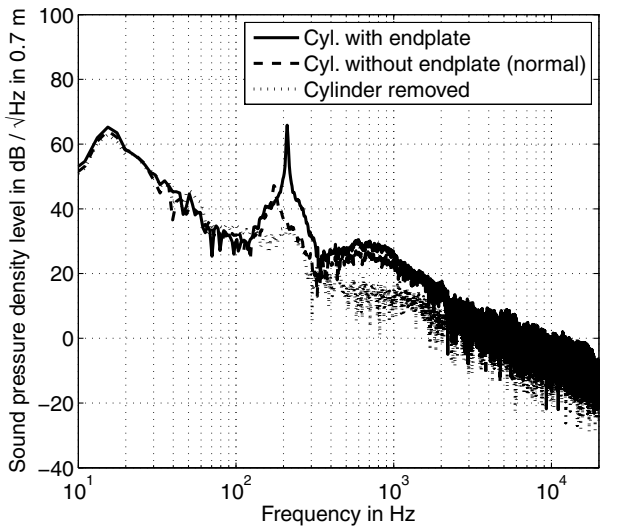

Fig. 56 Influence of the end plate on flow-induced sound of a wall-mounted square cylinder with a short wedge in front at $U_0 = 30$ m/s in the narrowband spectrum.

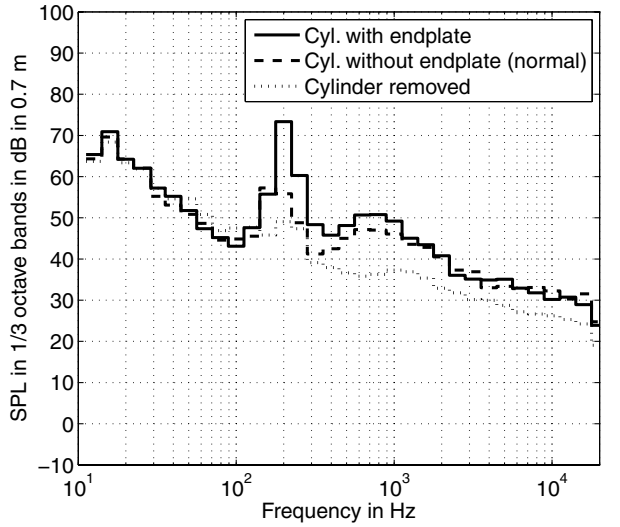

Fig. 57 Influence of the end plate on flow-induced sound of a wall-mounted square cylinder with a short wedge in front at $U_0 = 30$ m/s in one-third-octave bands.

that the increase in the flow-induced sound when an end plate is added is less than in the case of the unmodified square cylinder. The magnitude of the aeolian tone rises by only about 6 dB and the frequency of the vortex shedding changes only slightly from 103 to 98 Hz (see Table 2); that is, whether an end plate is present or not makes less difference than in the case of the basic square cylinder.

The results shown in Figs. 54 and 55 are in agreement with the statement that the roof vortex has a major influence on the development of the vortex street. Using a cylinder with an elliptical afterbody leads to the almost complete reattachment of the roof vortex, allowing the vortex street to develop virtually undisturbed. With the help of an end plate, the roof vortex is completely suppressed. Little extra stability is gained for the vortex street, resulting in only a slight increase in both tonal and broadband noise. The slight higher broadband-noise level can be caused by flow interaction with the additional end plate on the roof.

C. Square Cylinder with a Short Wedge Added in Front

Similar results are obtained for the third configuration, consisting of a square cylinder with a short wedge added in front. In its unmodified setup without an end plate, it is observed that a roof vortex is present that is of smaller size than at the reference square cylinder. Therefore, its complete suppression should lead to a limited increase in the flow-induced sound. As can be seen in Figs. 56 and 57, the magnitude of the aeolian tone rises by about 14 dB and the shedding frequency changes from 174 to 211 Hz (see also Table 2).

D. Summary of the Influence of the Roof Vortex on Flow-Induced Sound

Table 2 summarizes the findings of this section. If a roof vortex is present in the unmodified configuration, its removal leads to a significant increase in flow-induced sound because then the vortex street can develop undisturbed (i.e., configurations with a square cylinder and a square cylinder with a wedge in front). However, if in the basic configuration the roof vortex interferes only weakly with the vortex street, its suppression results in only minor increases in flow-induced sound (i.e., configuration with a square cylinder with an elliptical afterbody).

VI. Conclusions

The influence of geometry variations on flow-induced sound is demonstrated for the case of a wall-mounted square cylinder. Its radiation characteristic is a dipolelike behavior, as in the case of a

two-dimensional circular cylinder. Pressure fluctuations on opposite cylinder faces not incident to the flow are in phase opposition, in addition to sound signals observed from the same directions. The directivity is close to a dipole pattern, although maximum levels are shifted slightly toward the direction of the flow.

The wall-pressure fluctuations are not homogeneously distributed along the cylinder's axis. As also found in the distribution of turbulent kinetic energy, fluctuations are higher near the base of the cylinder.

Changes in geometry influence the amount of flow-induced sound. Adding the elliptical half-body downstream of the cylinder increases the aeolian tone by about 13 dB. However, the amount of turbulence in the flow and the coefficient of drag are reduced: that is, reductions in turbulence do not necessarily have to imply lower sound levels. When the short wedge is added instead, both turbulence and induced sound are reduced. The same kind of variations are found in the local wall pressures of the investigated geometries. Larger fluctuation levels and longer correlation lengths correspond to increases in the aeolian tone.

The distribution of turbulence among the individual velocity components also seems to play an important role. When the flow, especially in the mean flow direction, is dominated by fluctuations in one velocity component only (e.g., a square cylinder with an elliptical half-body downstream), then the largest amount of noise is observed. If, however, the turbulent kinetic energy is distributed more evenly among the velocity components (e.g., a square cylinder with a wedge in front), then the least amount of flow-induced sound is observed. Therefore, information about the magnitude of turbulent energy k alone is not sufficient to estimate the radiated sound field. Drag reduction does not lead automatically to a decrease in flow-induced sound, as observed in the wall-mounted obstacles investigated.

Because of the three-dimensional setup, the flow can pass over the cylinder's top. The development of the vortex street is strongly influenced by the roof vortex. In its absence, the vortex street can develop undisturbed, as in the setup consisting of the square cylinder with the elliptical afterbody. The influence of the roof vortex on both vortex street and induced sound is underlined in additional experiments. Using an end plate to suppress the roof vortex results in a significant increase in flow-induced sound (in some cases, by more than 20 dB), if a roof vortex was present before.

Flow instabilities created by a leading wedge destroy the symmetry of the vortex street. Although the roof vortex is smaller in that particular case, the vortex street is disturbed mainly by flow instabilities due to the leading wedge.

From the measurements conducted, one can conclude that it is advantageous to break up the symmetry of the vortex street and reduce its stability, to keep fixed separation lines and to inhibit fluctuations of the upstream stagnation line to obtain reductions of flow-induced sound, among other known approaches.

Acknowledgment

The funding of this work was provided by the Bayerische Forschungsstftung (Bavarian Research Foundation), Munich, Germany, which is greatly appreciated.

References

[1] Blake, W. K., "Mechanics of Flow-Induced Sound and Vibration," Vol. 1, Academic Press, New York, 1986.

[2] Phillips, O. M., "The Intensity of Aeolian Tones," *Journal of Fluid Mechanics*, Vol. 1, No. 6, 1956, pp. 607–624.

[3] Naudascher, E., and Rockwell, D., "Flow-Induced Vibrations," A.A. Balkema, Rotterdam, The Netherlands, 1994.

[4] Bruun, H. H., *Hot-Wire Anemometry*, Oxford Univ. Press, Oxford, 1995.

[5] Zdravkovich, M. M., *Flow Around Circular Cylinders*, Oxford Univ. Press, Oxford, 1997.

[6] Norberg, C., "Fluctuating Lift on a Circular Cylinder: Review and New Measurements," *Journal of Fluids and Structures*, Vol. 17, No. 1, 2003, pp. 57–96.

[7] Bearman, P. W., "Vortex Shedding from Oscillating Bluff Bodies," *Annual Review of Fluid Mechanics*, Vol. 16, 1984, pp. 195–222.

[8] Norberg, C., "Flow Around Rectangular Cylinders: Pressure Forces and Wake Frequencies," *Journal of Wind Engineering and Industrial Aerodynamics*, Vol. 49, Nos. 1–3, Pt. 1, 1993, pp. 187–196.

[9] Knisely, C. W., "Strouhal Numbers of Rectangular Cylinders at Incidence: A Review and New Data," *Journal of Fluids and Structures*, Vol. 4, No. 4, 1990, pp. 371–393.

[10] Dutta, S., Muralidhar, K., and Panigrahi, P. K., "Influence of the Orientation of a Square Cylinder on the Wake Properties," *Experiments in Fluids*, Vol. 34, No. 1, 2003, pp. 16–23.

[11] Fujita, H., Sha, W., Furutani, H., and Suzuki, H., "Experimental Investigations and Prediction of Aerodynamic Sound Generated from Square Cylinders," AIAA Paper 98-2369.

[12] Wang, H. F., Zhou, Y., Chan, C. K., Wang, W. O., and Lam, K. S., "Flow Structure Around a Finite-Length Square Prism," *Proceedings of AFMC15* [CD-ROM], Univ. of Sydney, Sydney, Australia, Sept. 2004.

[13] Sakamoto, H., "Vortex Shedding from a Rectangular Prism and a Circular Cylinder Placed Vertically in a Turbulent Boundary Layer," *Journal of Fluid Mechanics*, Vol. 126, No. 1, 1983, pp. 147–165.

[14] Becker, S., Lienhart, H., and Durst, F., "Flow Around Three-Dimensional Obstacles in Boundary Layers," *Journal of Wind Engineering and Industrial Aerodynamics*, Vol. 90, Nos. 4–5, 2002, pp. 265–279.

[15] Kaltenbacher, M., Escobar, M., Hahn, C., Ali, I., and Becker, S., "CAA as a Postprocessing Step Within CFD Computations," International Conference on Noise & Vibration Engineering Paper 435, Sept. 2006.

[16] Escobar, M., Ali, I., Hahn, C., Kaltenbacher, M., and Becker, S., "Investigation of Acoustic Sources for a FV/FE Coupled Computation Using Different Grids," 11th AIAA Aeroacoustics Conference, AIAA Paper 2005-3017 May 2005.

[17] Mijata, M., and Hayashi, Y., "Aerodynamic Sound Emitted from a Rectangular Bar with Rounded Edge(s) in Uniform Flow," *Proceedings of ICSV13* [CD-ROM], Vienna Univ. of Technology, Vienna, Austria, July 2006.

[18] Hayashi, Y., Kodama, Y., and Fukano, T., "Sound Generation from Tapered Cylinder," *Proceedings of ICSV13* [CD-ROM], Vienna Univ. of Technology, Vienna, Austria, July 2006.

[19] You, D., Choi, H., Choi, M.-R., and Kang, S.-H., "Control of Flow-Induced Noise Behind a Circular Cylinder Using Splitter Plates," *AIAA Journal*, Vol. 36, No. 11, 1998, pp. 1961–1967.

[20] Blake, W. K., *Mechanics of Flow-Induced Sound and Vibration*, Vol. 2, Academic Press, New York, 1986.

[21] Takaishi, T., "Method of Evaluating Dipole Sound Source in Finite Computational Domain," *Journal of the Acoustical Society of America*, Vol. 113, No. 3, 2004, pp. 1427–1435.

[22] Bendat, J. S., and Piersol, A. G., *Random Data Analysis and Measurement Procedures*, Wiley, New York, 1986.

[23] Uffinger, T., "Untersuchungen der Geschwindigkeits- und Turbulenzverteilung bei der Umströmung Verschiedener Wandgebundener Zylinderstumpfgeometrien," B.S. Thesis, Dept. of Fluid Mechanics, Univ. of Erlangen—Nürnberg, Erlangen, Germany, 2006.

[24] Miles, J., "Aligned and Unaligned Coherence: a New Diagnostic Tool," NASA TM-2006-214112, 2006.

[25] Hucho, W.-H., *Aerodynamik des Automobils*, 5th ed., Vieweg–Verlag, Wiesbaden, Germany, 2005.

[26] Bechara, W., Bailly, C., and Lafon, P., "Stochastic Approach to Noise Modeling for Free Turbulent Flows," *AIAA Journal*, Vol. 32, No. 3, 1994, pp. 455–463.

[27] Ewert, R., Delfs, J., and Lummer, M., "The Simulation of Airframe Noise Applying Euler-Perturbation and Acoustic Analogy Approaches," *International Journal of Aeroacoustics*, Vol. 4, Nos. 1–2, 2005, pp. 69–91.

[28] Marsden, A. L., Wang, M., Denis, J. E., Jr., and Moin, P., "Trailing Edge Noise Reduction Using Derivate-Free Optimization and Large Eddy Simulation," *Journal of Fluid Mechanics*, Vol. 572, No. 2, 2007, pp. 13–36.

[29] Oberai, A. A., Roknaldin, F., and Hughes, T. J. R., "Computation of Trailing Edge Noise Due to Turbulent Flow over an Airfoil," *AIAA Journal*, Vol. 40, No. 11, 2002, pp. 2206–2216.

[30] Brooks, T. F., and Hodgson, T. H., "Trailing Edge Noise Prediction from Measured Surface Pressure," *Journal of Sound and Vibration*, Vol. 78, No. 1, 1981, pp. 69–117.

[31] Hahn, C., "Experimentelle Analyse und Reduktion Aeroakustischer Schallquellen an Einfachen Modellstrukturen," Ph.D. Thesis, Univ. of Erlangen—Nürnberg, Erlangen, Germany, 2008.

C. Bailly
Associate Editor